Jupiter's unearthly jets: a new turbulent model exhibiting statistical steadiness without large-scale dissipation

Stephen I. Thomson, Michael E. McIntyre

Department of Applied Mathematics and Theoretical Physics, University of Cambridge, UK

www.damtp.cam.ac.uk/user/sit23/, stephen.i.thomson@gmail.com; www.damtp.cam.ac.uk/user/mem2/, mem2@cam.ac.uk

Submitted to *J. Atmos. Sci.*, 9 December 2014

ABSTRACT

A longstanding mystery about Jupiter has been the straightness and steadiness of its weather-layer jets, quite unlike terrestrial strong jets with their characteristic unsteadiness and long-wavelength meandering. The problem is addressed in two steps. The first is to take seriously the classic Dowling–Ingersoll $1\frac{1}{2}$-layer scenario and its supporting observational evidence. The evidence implies the existence of deep, massive, zonally-symmetric zonal jets in the underlying dry-convective layer. There is then the possibility of straight, stable weather-layer jets with the deep jets acting as guide-rails. Stability is possible even with nonmonotonic weather-layer potential-vorticity gradients. The second step is to improve the realism of the small-scale stochastic forcing used to represent Jupiter's moist convection, as far as possible within the $1\frac{1}{2}$-layer dynamics. The real, three-dimensional moist convection should be strongest in the belts where the interface to the deep flow is highest and coldest. It is likely, moreover, to generate cyclones as well as anticyclones but with the anticyclones systematically stronger. Such forcing can act quasifrictionally on large scales, and thus produce statistically steady turbulent weather-layer regimes without artificial large-scale friction. Forcing strengths sufficient to produce chaotic vortex dynamics can also produce realistic belt–zone contrasts in the model's moist-convective activity, through a tilting of the interface by eddy-induced sharpening and strengthening of the weather-layer jets relative to the deep jets. Weaker forcing for which the only jet-sharpening mechanism is the passive (Kelvin) shearing of vortices, the so-called "CE2" or "SSST" or "zonostrophic instability" mechanism, produces unrealistic belt–zone structures.

1. Introduction

The goal of this work is to find the simplest nontrivial model of Jupiter's visible weather layer that reproduces the straightness and steadiness of the observed prograde jets. The weather layer is the cloudy, moist-convective layer overlying a much deeper, hotter dry-convective layer. Such vertical structure, though not directly observed, is to be expected from the need to carry a substantial heat flux from below and from the basic thermodynamics and estimated chemical composition of Jupiter's atmosphere (e.g., Sugiyama et al. 2006, and references therein).

Even at high latitudes, the observed weather-layer jets are "straight" in the sense that they closely follow latitude circles, as dramatically shown in the well known synthetic polar view from Cassini images.[1] The jets are also remarkably close to being steady, as evidenced by the almost identical zonal-mean zonal wind profiles seen in 1979 and 2000, from cloud tracking in the Voyager 1 and Cassini images (Limaye 1986; Porco et al. 2003). Because the weather layer appears turbulent and has no solid lower boundary, we seek a model that can reach statistically steady states in the absence of large-scale friction. We also avoid the use of large-scale Newtonian cooling. Real radiative heat transfer is not only far more complicated, but also dependent on unknown details of the cloud structure within the weather layer and near the interface with the dry-convective layer.

The straightness and steadiness of Jupiter's prograde jets makes them strikingly dissimilar to the strong jets of the Earth's atmosphere and oceans, with their typical longwave meandering. By strong jets we mean the atmosphere's tropopause and polar-night jets, and the strongest ocean currents such as the Gulf Stream, the Kuroshio and the Agulhas. The cores of these terrestrial strong jets are marked by concentrated isentropic gradients of Rossby–Ertel potential vorticity or gradients of ocean surface temperature, inversion of which implies sharp velocity profiles having width scales of the order of an appropriate Rossby deformation lengthscale L_{D}. Such meandering strong jets, which also appear in single-layer "beta-turbulence" models of Jupiter's weather layer when L_{D} values are realistic, and when forcing and dissipation are both small enough (e.g., Scott and Polvani 2007; Scott and Dritschel 2012), are

[1] A movie is available from www.nasa.gov/mission_pages/cassini/ /multimedia/pia03452_prt.htm or more directly from http://www.ciclops.org/view_media/367/Jupiter-Polar-Winds

quite different from the straighter but very weak "ghost" or "latent" jets in the Pacific ocean, visible only after much time-averaging (Maximenko et al. 2005, & references therein).

Jupiter's jets are hardly weak. On the contrary, at least some of them are strong enough to look shear-unstable, by some criteria, with nonmonotonic potential-vorticity gradients (e.g., Dowling and Ingersoll 1989; Read et al. 2006; Marcus and Shetty 2011). Here we argue that their straightness and steadiness may come from a different, strictly extraterrestrial combination of circumstances, which moreover are incompatible with standard "beta-turbulence" models of the weather layer.

We propose a new idealized model whose two most crucial aspects are as follows. The first is the stochastic forcing of turbulence by thunderstorms and other small-scale moist-convective elements injected into the weather layer from the underlying dry-convective layer.[2] We assume that moist convection generates small cyclones and anticyclones, with a bias toward stronger anticylones. Such a "potential-vorticity bias" or "PV bias" recognizes that heat as well as mass is injected. This contrasts with the mass-only, anticyclonic-only scenarios of Li et al. (2006) and Showman (2007) on the one hand, and with the perfectly unbiased small-scale forcing used in standard beta-turbulence models on the other. PV bias will enable us to dispense with the large-scale friction required in beta-turbulence models.

The second aspect is the presence of zonally-symmetric deep zonal jets in the underlying dry-convective layer. They will prove crucial to our model's behavior. Here we follow the pioneering work of Dowling and Ingersoll (1989, hereafter DI), who produced cloud-wind evidence pointing to two remarkable and surprising conclusions. The first is that the large-scale vortex dynamics, in latitudes around 15°–35° at least, is approximately the same as the dynamics of a potential-vorticity-conserving $1\frac{1}{2}$-layer model, with the upper layer representing the entire weather layer. DI's second conclusion is that the cloud-wind data can be fitted into this picture only if the underlying dry-convective layer is in large-scale relative motion. The simplest possibility allowing a good fit is that the relative motion consists of deep zonally-symmetric zonal jets. Those deep jets must have substantial velocities, comparable in order of magnitude to jet velocities at cloud-top levels. To our knowledge, no subsequent cloud-wind study has overturned this second conclusion. So we use a $1\frac{1}{2}$-layer model with deep jets. We treat the deep jets as prescribed and steady, consistent with the far greater depth and mass of the dry-convective layer.

The relevance of $1\frac{1}{2}$-layer dynamics has recently gained support from a different direction. Sugiyama et al. (2014) present results from a two-dimensional cloud resolving model that includes the condensation and precipitation of water and other minor species. A model weather layer emerges whose stable stratification is sharply concentrated near the interface with the dry-convective layer, as a consequence of water-cloud behavior. This result suggests that the real weather layer could be surprisingly close to the $1\frac{1}{2}$-layer idealization with its perfectly sharp interface. Further such work is needed, if only because the real cloud-scale moist convection must itself be three-dimensional, as suggested by the morphology both of Jupiter's folded filamentary regions and of terrestrial supercell or "tornado alley" thunderstorms, with their intertwined patterns of updrafts, downdrafts, and precipitation.

DI's evidence for deep jets remains important today because, as yet, there are no other observational constraints on the existence or nonexistence of the deep jets, outside the equatorial region. No such constraints are expected until, hopefully, gravitational data come in from the Juno mission in 2016. Numerical models of the dry-convective layer cannot address the question because they need to make speculative assumptions about conditions at depth, including the effective bottom boundary conditions felt by Taylor-Proudman-constrained deep jets at latitudes within the associated tangent cylinder. Here there is great uncertainty. There is a range of possible conditions whose extremes are a slippery radiative layer well above the metallic-hydrogen transition, making deep jets easy to generate, and a no-slip magnetohydrodynamic transition layer that inhibits them (e.g., Guillot 2005; Jones and Kuzanyan 2009; Liu et al. 2013; Gastine et al. 2014, and references therein). Jupiter's prograde equatorial jet system needs separate consideration, being almost certainly outside any relevant tangent cylinder or cylinders.

Zonal symmetry or straightness is a plausible possibility for any deep, dry-convective jets that may exist, in virtue of the scale separation between the jets themselves and the relatively tiny, Coriolis-constrained convective elements that excite them (e.g., Jones and Kuzanyan 2009; Gastine et al. 2014, and references therein).

Our own relatively modest aim, then, is to see whether, on the basis of the DI scenario with prescribed deep, straight jets, an idealized $1\frac{1}{2}$-layer model can produce not only statistical steadiness in the absence of large scale dissipation but also realistic large scale weather-layer structures, with moist convective forcing strongest in the cyclonically-sheared "belts" and weakest in the anticyclonically-sheared "zones". The folded filamentary regions and lightning observed on the real planet, assumed to be symptomatic of moist convection, are concentrated in the belts (e.g., Porco et al. 2003). In addition we aim to test the effectiveness,

[2] We deliberately exclude other excitation mechanisms. In particular, we exclude terrestrial-type baroclinic instabilities. These are arguably weak or absent because of the absence of a solid lower surface at the base of the weather layer, and because of the weak pole-to-equator temperature gradient — a weakness expected, in turn, from the well known "convective thermostat" argument (Ingersoll and Porco 1978).

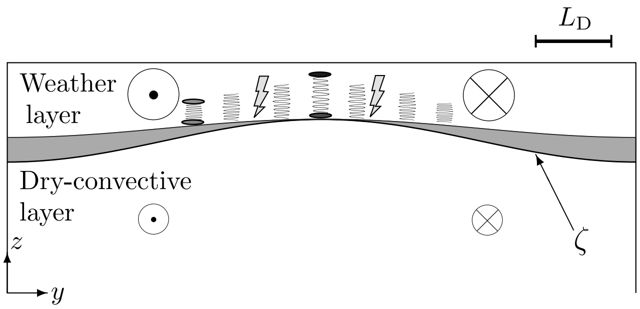

FIG. 1. Schematic of the model setup and motivation; see text. The bar at top right shows a typical L_D value. The notional cumulonimbus clouds, concentrated in the model belt, can be thought of as tending to generate vortex pairs with cyclones below and anticyclones above. Such vortex pairs, called "hetons" or "heatons" in the oceanographic literature, can tilt and then propagate like ordinary two-dimensional vortex pairs, which latter are all that can be accommodated in a $1\frac{1}{2}$-layer model. Ingersoll et al. (2000) remind us that "both cyclonic and anticyclonic structures exist within the belts" of the real planet, and succinctly summarize the case for their being generated by moist convection.

within the idealized model, of the "beta-gyre-mediated" migration of small anticyclones from belts into zones, following a suggestion by Ingersoll et al. (2000) that such migration might be significant.

We also aim to test whether and how the system might be held close to marginal shear stability, in a manner related to Arnol'd's second stability criterion ("A2 stability"), following a suggestion by Dowling (1993) and Stamp and Dowling (1993). We argue that jet straightness implies that Jupiter is either marginal or submarginal and that, despite nonmonotonic potential-vorticity gradients, submarginal is the more likely, as suggested by Ingersoll and Cuong (1981). Slightly supermarginal states are unlikely because they first go unstable at the longest available zonal wavelengths, which then equilibrate to a gentle, phase-coherent long-wave undulation of adjacent jets that would be conspicuous on the real planet but is not observed. Such coherent long-wave undulation has been well verified by us in slightly-supermarginal, unforced model runs, as well as being expected from instability theory.

The plan of the paper is as follows. Section 2 introduces the model. Section 3 introduces the PV-biased forcing and shows how it can act quasifrictionally. Section 4 motivates our choice of parameters, emphasizing those choices that lead to realistic weather-layer structures. Section 5 surveys the main body of results. Section 6 discusses the vortex-interaction mechanisms that produce realistic structures. We find that the migration mechanism is important. Section 7 shows that another much-discussed mechanism — the Kelvin passive-shearing mechanism (Thomson 1887), also called "CE2" or "SSST" (e.g., Srinivasan and Young 2014, and references therein) — has interesting effects but is unable to produce realistic weather-layer structures in our model. Section 8 presents some concluding remarks and a suggestion for future work.

2. Model formulation

We use a doubly-periodic, quasi-geostrophic, pseudo-spectral β-plane version of the $1\frac{1}{2}$-layer model, with leapfrog timestepping and a weak Robert filter. The model tries to mimic conditions in a band of northern-hemispheric latitudes containing two deep jets, one prograde and one retrograde. The simplest way to achieve shear-stability properties resembling those of a horizontally larger domain (Thomson 2015) is to choose the model's zonal (x) to latitudinal (y) aspect ratio to be 2:1. In most runs a 512×256 spatial grid is used. Further detail is in Thomson (2015), and an annotated copy of the code is provided online through the authors' websites.

Figure 1 shows schematically a meridional slice through the model, with the upper or weather-layer jets shown stronger than the deep jets and the interface correspondingly tilted, as dictated by thermal-wind balance, with elevation ζ say. The y-axis points northward and the x-axis eastward, out of the paper. The central raised, i.e., cold, interface is in a model belt, cyclonically sheared, with model zones on either side and with the whole structure repeated periodically. The underlying dry-convective layer is modeled as adiabatic and infinitely deep, with constant potential temperature θ. The constant-θ interface with the weather layer is the lower of the two curves shown. The interface is flexible, and responsive to the dynamics. The upper curve, above the shading, denotes the lifting condensation level (LCL) for water. Such a configuration is consistent with thermal-wind balance and with the standard perception that the weather layer's stable stratification — a positive vertical gradient $\partial\theta/\partial z$ — results from moist convection with the convection strongest in the belts, where the LCL is raised closest to the level of free convection.

The model equations for $q(x, y, t)$, the weather layer's large-scale quasi-geostrophic potential vorticity (PV), with forcing $F(x, y, t)$ and small-scale dissipation $D(x, y, t)$, are

$$\left(\frac{\partial}{\partial t} + \mathbf{u}\cdot\nabla\right) q \;=\; F + D\,, \tag{2.1}$$

$$q \;:=\; \nabla^2\psi + \beta y - k_D^2\left(\psi - \bar{\psi}_{\text{deep}}\right). \tag{2.2}$$

Here ∇^2 is the two-dimensional Laplacian in the xy plane, β is the local latitudinal gradient of the vertical component of the planetary vorticity, k_D is the reciprocal of the Rossby deformation length L_D based on the weather-layer's mean depth and on g', the reduced gravity at the interface; $\psi(x, y, t)$ and $\mathbf{u}(x, y, t)$ are the geostrophic streamfunction and velocity for the weather layer, such that $\mathbf{u}$ is horizontal with components $\mathbf{u} = (u,\, v) = (-\partial\psi/\partial y,\; \partial\psi/\partial x)$, and $\bar{\psi}_{\text{deep}}$ is the geostrophic streamfunction for the prescribed steady, zonally-symmetric zonal flow $\bar{u}_{\text{deep}} = -\partial\bar{\psi}_{\text{deep}}/\partial y$ in the dry-convective layer. D is a quasi-hyperdiffusive dissipation in the form of a high-wavenumber spectral filter, used only to maintain numerical stability. It will be ignored in most of the theoretical discussion. We adopt the filter described in appendix B of Smith et al. (2002). The model code evaluates $\nabla\psi$ and ∇q in spectral space before FFT-transforming to physical space and evaluating $\mathbf{u}\cdot\nabla q$ by pointwise multiplication, then transforming back.

Following Dowling (1993) and Stamp and Dowling (1993), we somewhat arbitrarily take the deep flow to have a sinusoidal profile

$$\bar{u}_{\rm deep}(y) \;=\; U_{\max}\sin\left(\frac{y}{L}\right) + U_0\,, \qquad (2.3)$$

where $U_{\max}$ and U_0 are constants. The lengthscale L is $(2\pi)^{-1}$ times the domain's y-period, the full wavelength of the jet spacing, which we fix at 10,000 km to represent mid-latitude conditions.

The real deep-jet profiles may of course be different. However, they are not well known. DI's analysis did, to be sure, find rounded $\bar{u}_{\rm deep}(y)$ profiles, in striking contrast with the sharper profiles found in some dry-convective models. However, DI's cloud-wind analysis may not have been accurate enough to fix $\bar{u}_{\rm deep}(y)$ with great precision. While cloud-wind analyses have greatly improved since then — see especially Asay-Davis et al. (2009) — we are not aware of any corresponding published estimates of $\bar{u}_{\rm deep}(y)$ profiles and their error bars.

With the exception of q, which contains the non-periodic terms $\beta y - k_{\rm D}^2 U_0 y$, all the model's weather-layer fields are assumed to be doubly periodic including the streamfunction ψ and the zonal-mean gradient $\partial\bar{q}/\partial y$ of q,

$$\frac{\partial\bar{q}}{\partial y} \;=\; \beta - \frac{\partial^2\bar{u}}{\partial y^2} + k_{\rm D}^2\left(\bar{u}-\bar{u}_{\rm deep}\right)\,. \qquad (2.4)$$

The periodicity of ψ entails that

$$\int_0^{2\pi L}\bar{u}\,dy = 0\,, \qquad (2.5)$$

which implicitly assumes not only that we are in a particular reference frame, but also that the domain-averaged angular momentum budget is steady.[3] And without loss of generality we may take the domain integrals of ψ and F to vanish:

$$\iint\psi\,dxdy = 0\,, \qquad \iint F\,dxdy = 0\,. \qquad (2.6)$$

The first of these follows from the freedom to add an arbitrary function of time t alone to the streamfunction ψ, with no effect on the quasi-geostrophic dynamics. Physically, this says that a small variation in the total mass of the weather layer, due for instance to horizontally-uniform diabatic processes, has no dynamical effect as long as the mean weather-layer depth, hence $L_{\rm D}$ value, can be considered constant to leading order in Rossby number. From (2.2) and the first of (2.6) we then have

$$\frac{\partial}{\partial t}\iint q\,dxdy \;=\; 0\,, \qquad (2.7)$$

which is consistent with (2.1) only if the second of (2.6) also holds. This can be seen by domain-integrating the flux form of (2.1) and noting that $\bar{v} = \partial\bar{\psi}/\partial x = 0$, and that $\iint D\,dxdy = 0$ in virtue of D's restriction to the highest wavenumbers. It is convenient to view (2.7) as a quasi-geostrophic counterpart to the "impermeability theorem" for the exact, Rossby–Ertel PV (e.g., Haynes and McIntyre 1990).

From here on we ignore the small-scale dissipation D. The zonal-mean dynamics is then described by

$$\frac{\partial\bar{q}}{\partial t} \;=\; -\frac{\partial(\overline{v'q'})}{\partial y} + \bar{F}\,, \qquad (2.8)$$

where the primes denote departures from zonal averages $\overline{(\;)}$. The model's Taylor identity (e.g., Bühler 2014), which allows the mean PV dynamics to be translated into mean momentum dynamics, if desired,[4] is

$$\frac{\partial(\overline{u'v'})}{\partial y} \;=\; -\overline{v'q'}\,. \qquad (2.9)$$

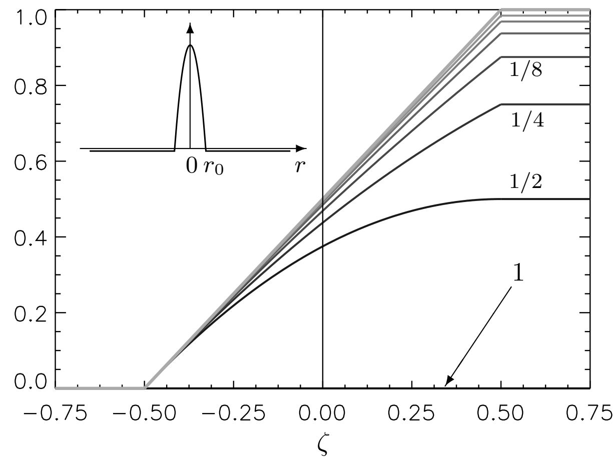

FIG. 2. Functions used in the vortex-injection scheme. The inset at top left shows the $\Delta q(r)$ profile for an injected cyclone of radius $r_0 \ll L_{\rm D}$. The profile has a central parabolic portion given by Eq. (3.1), to which is added a small negative constant such that the domain integral $\iint\Delta q(r)\,dxdy = 0$, the artificial "complementary forcing" needed to maintain consistency with (2.6) and (2.7). For an anticyclone, all signs are reversed. The main figure shows the functions of ζ used in (3.4)–(3.8) to determine the injection strengths. The different curves correspond to different choices of bias. From bottom up we have $b = 1$ (value is zero for all ζ) and then $b_{\max} = 1/2$, 1/4, 1/8, 1/16, 1/32, 1/64, 0. The topmost, lightest curve $b_{\max} = 0$ corresponds to the ramp function $\rho(\zeta)$ in (3.6).

[3] In other words, any domain-averaged external zonal force is either negligible or balanced by a domain-averaged ageostrophic mean y-velocity.

[4] The mean momentum dynamics is given by the indefinite y-integral of (2.8), in which $-k_{\rm D}^2\int\partial\bar{\psi}/\partial t\,dy$ represents the Coriolis force from the ageostrophic mean y-velocity.

The Taylor identity is a consequence of (2.2) alone, as is easily verified using $\partial\overline{(\ )}/\partial x = 0$, hence valid at all eddy amplitudes and independent of forcing and dissipation. By multiplying (2.1) by $-\psi$, and continuing to ignore D, we find the relevant energy equation to be

$$\frac{\partial E}{\partial t} \;=\; -\iint \psi F \,dxdy \tag{2.10}$$

where E is the kinetic plus available potential energy of the weather layer — the model's only variable energy — divided by the mass per unit area. That is,

$$E \;:=\; \iint \left(\tfrac{1}{2}|\nabla\psi|^2 + \tfrac{1}{2}k_{\rm D}^2\psi^2\right) dxdy\;. \tag{2.11}$$

3. The forcing F

The forcing F corresponds to repeated injections of close-spaced, east-west-oriented pairs of small vortices at random locations and in alternating order, cyclone-anticyclone alternating with anticyclone-cyclone. In each pair, the cyclone is weaker than the anticyclone by a fractional amount b, say, which we call the "fractional bias", and which increases with vortex strength so as to express the notion that the dry-convective layer supplies the weather layer with mass and heat but with relatively more mass in the stronger convection events. Each vortex is impulsively injected using the parabolic PV profile shown in the inset to Fig. 2. We acknowledge that this must be an exceedingly crude representation of vortex generation by the real three-dimensional convection, whose structure and properties are unknown and have yet to be plausibly modeled. However, a simplistic vortex-injection scheme may be the best that can be done within the $1\frac{1}{2}$-layer dynamics, and indeed is a rather time-honored idea (e.g., Humphreys and Marcus 2007, Section 5a and Fig. 6).

We use east-west-oriented pairs for two reasons. One is to make zonally averaged quantities such as $\bar{q}$ and $\overline{v'q'}$ less noisy. The other, less obvious, reason is an interest in assessing whether the Kelvin passive-sheared-disturbance mechanism (also called "CE2" and "SSST" in the literature) has a significant role in any of the regimes we find. The Kelvin mechanism operates when the injected vortices are so weak that they are passively sheared by the mean flow $\bar{u}(y)$, producing systematically slanted structures and hence Reynolds stresses $\overline{u'v'}$ potentially able to cause jet self-sharpening by "zonostrophic instability". The Kelvin mechanism is entirely different from the inhomogeneous-PV-mixing mechanism that produces terrestrial strong jets, through drastic piecewise rearrangement of a background PV gradient. It is also different from the Rhines mechanism, in which the injected vortices are strong enough to undergo the usual vortex interactions, especially the merging or clustering that produces an upscale energy cascade that is then arrested, or slowed, by the Rossby-wave elasticity of an *un-rearranged* background PV gradient. We are of course interested in whether any of these mechanisms have significant roles. Regarding the Kelvin mechanism, it is strongest when the forcing is anisotropic in the sense of east-west vortex-pair orientation (e.g., Shepherd 1985; Srinivasan and Young 2014). So our choice of east-west orientation will give the Kelvin mechanism its best chance.

The impulsive vortex injections, corresponding theoretically to temporal delta functions in the forcing function F, are actually spread over time intervals $2\Delta t$ to avoid exciting the leapfrog computational mode, where Δt is the timestep. This is still fast enough for advection to be negligible, implying that the injections are instantaneous to good approximation. The parabolic profile of the resulting change $\Delta q(r)$ in the PV field is given by

$$\Delta q(r) \;=\; q_{\rm pk}\left(1-\frac{r^2}{r_0^2}\right) \quad (r \leqslant r_0)\;, \tag{3.1}$$

the peak vortex strength $q_{\rm pk}$ being positive for a cyclone and negative for its accompanying anticyclone. The relative radius $r := |\mathbf{x}-\mathbf{x}_{\rm c}|$ with $\mathbf{x} = (x, y)$ denoting horizontal position and $\mathbf{x}_{\rm c} = (x_{\rm c}, y_{\rm c})$ the position of the vortex center. The radius r_0 is taken as small as we dare, consistent with reasonable resolution and realistic-looking vortex interactions. In most cases $r_0 = 4\Delta x$ where Δx is the grid size.

Thanks to the peculiarities of quasi-geostrophic dynamics and to our model choices we need the forcing to satisfy (2.6b). The model code does this automatically, by assigning zero values to all spectral components having total wavenumber zero. The most convenient way to see what it means, however, is to think of each injected vortex as satisfying (2.6b) individually. When, for instance, a small anticyclone is injected, it is accompanied by a domain-wide cyclonic "complementary forcing", in the form of a small, spatially-constant contribution, additional to (3.1) and spread over the entire domain, such that $\iint F\,dxdy$ is zero. That is not to say that the *dynamical* response to a single injection is domain-wide. Rather, the complementary forcing is no more than a convenient bookkeeping device to guarantee that the forcing is consistent, at all times, with our choice of model setup including double periodicity, the choice (2.6), and its consequence (2.7).

Consider for instance a localized mass injection. The dynamical response is formation of an anticyclone, namely a negative anomaly in the q field together with the associated mass and velocity fields obtainable by PV inversion (e.g., Hoskins et al. 1985, and references therein). Those fields describe an outward mass shift and anticyclonically-circulating winds, the whole structure extending outwards and decaying exponentially on the lengthscale $L_{\rm D}$. The complementary forcing is quite different. It can be pictured as a uniform, domain-wide withdrawal of a compensating amount of mass, which is small of the order of the Rossby number, and which has no dynamical effect whatever. It is an artificial device to keep the mass of the model weather layer exactly constant. Of course with anticyclonic bias a domain-wide mass withdrawal would have to occur in reality, presuming statistical steadiness, and would involve radiative heat transfer (e.g., Li et al. 2006). However, that aspect of the problem is invisible to the quasi-geostrophic dynamics.

We have explored many vortex-injection schemes, with many choices of the way in which injected vortex strengths $|q_{\rm pk}|$ are made to vary with the interface elevation or coldness ζ. The simplest choices, with strengths increasing monotonically with ζ, produce runaway situations with vortices far stronger than the real planet's mean shears and observed vortices, incompatible with our aim of finding flow regimes that are both realistic and statistically steady.

After much experimentation, the following vortex-injection scheme proved successful, one aspect of which is that $|q_{\rm pk}|$ is never allowed to exceed a set value $q_{\rm max} > 0$. The sensitivity to interface elevation or coldness is set by a parameter $\psi_{\rm lim} > 0$, in terms of which the definition of ζ will be written as

$$\zeta(x, y, t) \;=\; \frac{\tilde{\psi}_{\rm deep}(y) - \psi(x, y, t)}{\psi_{\rm lim}} \,, \tag{3.2}$$

where

$$\tilde{\psi}_{\rm deep}(y) \;:=\; LU_{\rm max} \cos\left(\frac{y}{L}\right) \,, \tag{3.3}$$

corresponding to the y-oscillatory or jet-like part of the deep flow (2.3).[5] Injections are done one pair at a time, with the intervening time intervals selected at random from a specified range $[4\Delta t,\; t_{\rm max}]$, with uniform probability. The minimum value $4\Delta t$ ensures that injection events do not overlap in time. The maximum value $t_{\rm max}$ is usually chosen to be much larger, such that $\frac{1}{2}t_{\rm max}$, close to the average time interval, is of the same order as the background shearing time $L/U_{\rm max}$. We interpret these temporally sparse injections as idealizing the intermittency of real convection, probably governed by slow but chaotic dry-convective dynamics along with time-variable structure near the interface (e.g., Showman and de Pater 2005; Sugiyama et al. 2014).

For each injection event a location $\mathbf{x} = (x,\, y)$ is chosen at random and a close-spaced but non-overlapping pair of vortices, each of radius r_0 as specified in (3.1), is injected at the pair of neighboring points $(x_{\rm c},\, y_{\rm c}) = (x \pm \frac{1}{2}s,\; y)$ where the separation s is fixed at $s = 2r_0 + \Delta x$. We denote the respective strengths by $q_{\rm pk} = q_{\rm pkC} > 0$ for the cyclone and $q_{\rm pk} = q_{\rm pkA} < 0$ for the anticyclone, with magnitudes always in the ratio $B \leqslant 1$ where

$$B \;=\; \left|\frac{q_{\rm pkC}}{q_{\rm pkA}}\right| \;=\; (1 - b) \,. \tag{3.4}$$

The fractional bias b is either 1, to give anticyclones only, as in Li et al. (2006) and in Showman (2007), or

$$b \;=\; b(\zeta) \;=\; b_{\rm max}\, \rho(\zeta) \tag{3.5}$$

in all other cases, where $b_{\rm max} < 1$ is a positive constant and where $\rho(\zeta)$ is the three-piece ramp function shown as the top curve in the main part of Fig. 2. It is given by

$$\rho(\zeta) \;:=\; \tfrac{1}{2} + \zeta \quad (-\tfrac{1}{2} \leqslant \zeta \leqslant \tfrac{1}{2}) \tag{3.6}$$

with $\rho = 0$ for $\zeta \leqslant -\frac{1}{2}$ and $\rho = 1$ for $\zeta \geqslant \frac{1}{2}$.

It remains to choose how $|q_{\rm pkA}|$ varies. The simplest choice would be

$$|q_{\rm pkA}| \;=\; q_{\rm max}\, \rho(\zeta) \,. \tag{3.7}$$

It corresponds to the set of curves shown in the main part of Fig. 2, with $|q_{\rm pkA}|/q_{\rm max}$ at the top together with the corresponding $q_{\rm pkC}/q_{\rm max}$ curves implied by Eqs. (3.4)–(3.7) for values of $b_{\rm max} < 1$. The label 1 marks the anticyclones-only case $b = 1$. However, the choice (3.7) still produces runaway situations incompatible with statistical steadiness, except when $q_{\rm max}$ is made too small to produce significant small-scale vortex activity. For larger $q_{\rm max}$ values, enough to produce such activity, the typical behavior is the growth and unbounded strengthening of a large cyclone. The large cyclone's cold-interface footprint, still larger in area, induces strong local injections from which the small injected cyclone tends to migrate inward and the anticyclone outward to give a cumulative, and apparently unbounded, increase in the cyclone's size and strength. (Notice by the way that this mechanism is quite different from the classic vortex merging or upscale energy cascade. The possibility of an unbounded *increase* in vortex strength is another peculiarity of quasi-geostrophic theory, predicting its own breakdown as Rossby numbers increase.)

Large, strong cyclones have correspondingly large q' values, motivating our final choice, which is to use (3.7) whenever the local q' value satisfies

$$\max\left(B|q_{\rm pkA}| + q',\; |q_{\rm pkA}| - q'\right) \;\leqslant\; q_{\rm max} \tag{3.8}$$

whereas, if (3.7) gives a $|q_{\rm pkA}|$ value that makes the left-hand side of (3.8) greater than $q_{\rm max}$, then $|q_{\rm pkA}|$ is reduced just enough to achieve equality, i.e., reduced just enough to satisfy (3.8). The corresponding $q_{\rm pkC}$ is reduced by the same fractional amount, i.e., is given by (3.4) with B and b unchanged. The second argument of the max function

[5] Because of its double periodicity, our idealized model has no way of representing large-scale gradients in $\tilde{\psi}_{\rm deep}$ except insofar as $d\tilde{\psi}_{\rm deep}/dy = -\bar{u}_{\rm deep}$ enters the background PV gradient (2.4). Of course the model also ignores the real planet's other large-scale gradients, and associated mean meridional circulations, for instance large-scale gradients in temperature, in composition including hydrogen ortho–para fraction (e.g., Read et al. 2006, Fig. 10), and in the Coriolis parameter and $L_{\rm D}$.

in (3.8) covers the possibility that strong anticyclones with large negative q' might occur, though it is the first argument that prevails in all the cases we have seen.

The limitations thus placed on the strongest vortices injected are interpreted here as reflecting not only the limitations of quasi-geostrophic theory, but also the unknown limitations of the real, three-dimensional moist convection as a mechanism for generating coherent vortices on the larger scales represented by our model. On smaller scales one must expect three-dimensionally turbulent vorticity fields with still stronger peak magnitudes — as terrestrial tornadoes remind us — though, with no solid lower surface, the details are bound to be different. For one thing, net mass injection rates are bound to be modified by such phenomena as evaporation-cooled, precipitation-weighted thunderstorm downdrafts, also called microbursts, contributing negatively. The concluding remarks in Section 8 will suggest a possible way of replacing (3.8) by something less artificial, albeit paid for by further expanding the model's parameter space.

As mentioned earlier, the bias b has quasifrictional effects. These are most obvious in the zonal-mean dynamics described by (2.8), under the constraints (2.5)–(2.7). Because of thermal-wind balance and the positive slope of the ramp function $\rho(\zeta)$, the sign of $\bar{F}(y,t)$ tends on average to be anticyclonic in belts and cyclonic in zones whenever the upper or weather-layer jets are stronger than the deep jets (3.3), the case sketched in Fig. 1. The converse holds in the opposite case. So $\bar{F}$ tends on average to reduce differences between shears in the upper jets and in the deep jets. There is a corresponding quasifrictional effect on large cyclones. By contrast, fluctuations such as those giving rise to the eddy-flux term $-\partial(\overline{v'q'})/\partial y$ in (2.8) can act in the opposite sense, in some cases giving rise to realistic interface-temperature structures in the manner sketched in Fig. 1.

We find that the quasifrictional effects can be understood alternatively from environment-dependent negative contributions to the right hand side of the energy equation (2.10), competing with the positive, environment-independent "self-energy" inherent in each injection. This contrasts with the standard, perfectly unbiased forcing used in beta-turbulence theory (e.g., Srinivasan and Young 2012), which is designed such that the self-energy is the only contribution, allowing one to prescribe a fixed, positive energy input rate ε, which along with spectral narrowness is the normal prelude to using Kolmogorovian arguments. However, it would then be necessary to introduce a separate large-scale frictional term, as would be necessary also if cyclonic bias, $b < 0$, were to be used in our scheme. (Not surprisingly, taking $b < 0$ has antifrictional effects. When we tried it, the most conspicuous result was self-excitation of unrealistic long-wave undulations.)

When $\bar{F}$ and other quasifrictional effects with $b > 0$ are strong enough to produce realistic, statistically steady flow regimes, we find that upper-jet profiles tend to be pulled fairly close to deep-jet profiles. This tendency shows up robustly in test runs initialized with upper jets both weaker and stronger than the deep jets. In most cases, therefore, we use a standard initialization in which the upper-jet profiles are the same as the deep-jet profiles (3.3), making $\zeta = 0$ and the average forcing spatially uniform to start with. We then observe how the upper profiles and ζ change in response to the eddy flux $\overline{v'q'}$ in (2.8).

4. Parameter choices

It turns out that the interesting cases, statistically steady with realistic ζ or interface-temperature structure, occupy only a small region within the model's vast parameter space. Not surprisingly, the behavior is sensitive to $q_{\max}$ and L_{D} values, which govern the strength and nature of the model's vortex activity all the way from cases with no such activity — having only the Kelvin (CE2/SSST) passive-shearing mechanism — up to cases with vortex activity so violent as to disrupt the zonal structure altogether. It turns out that the Kelvin mechanism is unable to produce realistic ζ structure. See Section 7 below. The most interesting cases, our main focus, turn out to be those exhibiting chaotic vortex interactions just strong enough to make an impact on the y-profiles of $\overline{v'q'}$ in (2.8).

A big surprise, though, was that the behavior is very sensitive to the choice of $b_{\max}$, with the most interesting cases clustered around small values $\lesssim 10^{-1}$. This was especially surprising in view of the past work of Li et al. (2006) and Showman (2007) using purely anticyclonic forcing $b = 1$. The different behavior seems related in part to the absence of deep jets in their studies but presence in ours.

In considering choices of L_{D}, and remembering its latitude dependence, we would like to respect observational as well as theoretical constraints. However, observational constraints from the comet-impact waves are controversial and unclear.[6] Also, observational constraints from the DI work and its successors apply mainly to the lower latitudes of the Great Red Spot and other large anticyclonic Ovals, roughly 15°–35°. The original DI work appeared to be compatible with L_{D} values at, say, 35°S, that are very roughly in the range 1500–2250 km. The more recent work of Shetty and Marcus (2010), based on a much more sophisticated cloud-wind methodology, appears to constrain L_{D} values more tightly, for instance producing values close to 1900

[6] One reason is that even if the comet-impact waves were gravity waves guided by the weather layer they would have had a different structure in the underlying dry-convective layer, more like surface-gravity-wave structure than that of $1\frac{1}{2}$-layer dynamics. Another reason is the case made by Walterscheid (2000) that the observed comet-impact waves were in any case more concentrated in Jupiter's stratosphere.

km at latitudes around 33.5°S from an analysis of the flow around a large anticyclone, Oval BA. However, unlike DI, who used $1\frac{1}{2}$-layer primitive-equation dynamics, Shetty and Marcus (2010) assume that quasi-geostrophic $1\frac{1}{2}$-layer dynamics applies accurately to the real planet. In any case, it is likely that all these estimates apply to the locally deeper weather layer expected near large anticyclones, suggesting somewhat smaller values further eastward or westward, as well as further poleward in virtue of the increasing Coriolis parameter. Our approach will be to reserve judgement on these issues, and simply to find a range of $L_{\rm D}$ values for which the idealized model behavior looks realistic.

As indicated at the end of Section 1, an overarching requirement is to keep the model's jets straight by excluding long-wave shear instability. For upper jet profiles that are kept close to the deep-jet profiles (3.3) by $\bar{F}$ and its quasifrictional effect, the upper PV gradients $\partial\bar{q}/\partial y$ tend to be quite strongly nonmonotonic if we take plausible values of $U_{\rm max}$ and $\beta - k_{\rm D}^2 U_0$. Recall Eqs. (2.3)–(2.4), noting that the y-oscillatory part of the $k_{\rm D}^2$ term in (2.4) is small when the upper and lower jet profiles are close, that is, when $\bar{u}(y)$ is close to $\bar{u}_{\rm deep}(y) - U_0$.

If for instance we take $U_{\rm max} \simeq 30\,{\rm m\,s^{-1}}$ and $\beta - k_{\rm D}^2 U_0$ anywhere between the value zero suggested by DI's results and the value of β itself at the equator, $\simeq 5\times10^{-12}\,{\rm s^{-1}m^{-1}}$, then we get strongly nonmonotonic $\partial\bar{q}/\partial y$ essentially because, with $L = (2\pi)^{-1}\times 10^4 = 1592\,{\rm km}$, we have $\partial^2\bar{u}/\partial y^2$ values in the range $\pm U_{\rm max}/L^2 = \pm 12\times10^{-12}\,{\rm s^{-1}m^{-1}}$, whose magnitude is well in excess of β at any latitude.

The model's jet flow is then shear-unstable for sufficiently large $L_{\rm D}/L$, but stabilized when $L_{\rm D}/L$ is taken below some threshold of order unity. That threshold was recognized by Ingersoll and Cuong (1981) and, as pointed out by Dowling (1993), is related to the "A2 stabilization" described by Arnol'd's second stability theorem. It arises because reducing $L_{\rm D}/L$ reduces the intrinsic phase speeds and lateral reach of even the longest, hence fastest possible, pair of counterpropagating Rossby waves, each wave propagating upstream on adjacent prograde and retrograde jets. These reductions suppress the instability by "destroying the ability of the two Rossby waves to keep in step", with each wave holding its own against the mean flow (McIntyre and Shepherd 1987, p. 543; see also Hoskins et al. 1985, Fig. 18ff.). That is why the first wavelength to go unstable for slightly supermarginal $L_{\rm D}/L$ is the *longest* available wavelength, with zonal wavenumber $k_{\rm min}$, say. a fact that we have cross-checked in test runs with the unforced model showing, in addition, that the long waves equilibrate to a gentle undulation at small wave amplitude (Thomson 2015).

For unbounded or doubly-periodic domains the A2 theorem says that the flow is shear-stable if a constant c can be found such that

$$k_{\rm D}^2 + k_{\rm min}^2 > \frac{\partial\bar{q}/\partial y}{\bar{u}-c}\,, \qquad (4.1)$$

where as before $k_{\rm D}^2 := L_{\rm D}^{-2}$. For the sinusoidal profiles of our standard initialization, and for $\beta - k_{\rm D}^2 U_0 = 0$ as suggested by DI, it happens that (4.1), with $c = 0$, is a necessary as well as a sufficient condition for stability (Stamp and Dowling 1993). The right-hand side of (4.1) is then just L^{-2}, independent of $U_{\rm max}$, and the threshold is precisely at $k_{\rm D}^2 = L^{-2} - k_{\rm min}^2$.

In our model, with its 2:1 aspect ratio, we have $k_{\rm min}^2 = L^{-2}/4$. Therefore, $L_{\rm D} \lesssim (4/3)^{1/2}L = 1838\,{\rm km}$ should be enough to exclude long-wave shear instability, as long as the upper profiles $\bar{u}(y,t)$ stay close to the deep profiles $\bar{u}_{\rm deep}(y)$. It is arguable, however, that since the much larger domain of the real planet should correspond to $k_{\rm min}^2 \ll L^{-2}$, it might be more appropriate to take $L_{\rm D} \lesssim L = 1592$ km. Having regard to these considerations, we decided to use $L_{\rm D}$ values 1500 km or less in most of our model runs.

In the next two sections we describe and illustrate the model's behavior for $L_{\rm D} = 1200\,{\rm km}$ and $1500\,{\rm km}$ and for forcings strong enough to produce chaotic vortex interactions. In such cases the model robustly approaches stable, statistically steady states with fairly straight jets, and realistic ζ structures, over significant ranges of $q_{\rm max}$ and $b_{\rm max}$ and with nonmonotonic upper PV gradients $\partial\bar{q}/\partial y$.

We fix $U_{\rm max} = 35\,{\rm m\,s^{-1}}$ as a compromise between low and midlatitude values, and choose two values of $\beta - k_{\rm D}^2 U_0$, namely zero and $4.03\times10^{-12}\,{\rm s^{-1}m^{-1}}$. Both choices make $\partial\bar{q}/\partial y$ strongly nonmonotonic. The value zero requires prograde U_0, roughly consistent with DI's results; see their Fig. 4b and its idealization in Stamp and Dowling (1993). Prograde U_0 is in any case expected in latitudes outside a tangent cylinder of the dry-convective layer (e.g., Jones and Kuzanyan 2009). The value $4.03\times10^{-12}\,{\rm s^{-1}m^{-1}}$ is the value of β itself at latitude 35°. For convenience we refer to these two cases as "pure-DI" and "midlatitude" respectively, remembering, however, that nothing is known about actual U_0 values at the higher latitudes.

Because $\bar{F}$ tends to pull our model's upper jets more or less close to its deep jets, the strongest upper mean shears $\partial\bar{u}/\partial y$ tend to have orders of magnitude similar to that of the strongest deep shear $U_{\rm max}/L = 2.199\times10^{-5}\,{\rm s^{-1}}$. So a convenient dimensionless measure of $q_{\rm max}$ is

$$q_{\rm max}^* := \frac{q_{\rm max}}{U_{\rm max}/L}\,. \qquad (4.2)$$

The parameter $q_{\rm max}^*$ governs the likely fate of vortices injected into background shear of order $U_{\rm max}/L$. We take values ranging from $q_{\rm max}^* = 0.5$ up to $q_{\rm max}^* = 32$. At the low end of the range, practically all the injected vortices are shredded, i.e., sheared passively and destroyed. (There is still, of course, a quasifrictional $\bar{F}$ effect.) At the high end, the strongest injected vortices all survive even in adverse shear, e.g., anticyclones in cyclonic shear. In mid-range, one typically sees survival in favorable shear only. We call these three injection regimes "weak", "strong", and "semi-strong".

This behavior is consistent with the classic study of Kida (1981), allowing for Kida's different vortex profiles. In place of the parabolic profile (3.1), Kida used a top hat or "vortex patch" profile. Model test runs with single vortex injections behave qualitatively as expected from Kida's predictions when values of $\int_0^{r_0} \Delta q\, r\, dr$ are matched, identifying Kida's top-hat amplitude with $\frac{1}{2}|q_{\rm pk}|$. On that basis, Kida's condition for an anticyclone to survive in cyclonic shear translates to $q^*_{\rm max} > 13.443$ when $q_{\rm pkA} = -q_{\rm max}$, that is, for the strongest anticyclones then injected.[7] Kida's analysis is for $L_{\rm D} = \infty$ but should be qualitatively relevant when, as here, $r_0 \ll L_{\rm D}$.

The parameter $\psi_{\rm lim}$ in (3.2) has to be chosen empirically. We want the resulting ζ fields to range over values within, or slightly exceeding, the range $-\frac{1}{2} \leqslant \zeta \leqslant +\frac{1}{2}$ that corresponds to the sloping part of the ramp function $\rho(\zeta)$. A satisfactory choice is found to be $\psi_{\rm lim} = \Lambda q^*_{\rm max}$ where $\Lambda = 4.47 \times 10^6\,{\rm m^2 s^{-1}}$. This is used in all the runs shown here, all the way from $q^*_{\rm max} = 0.5$ to $q^*_{\rm max} = 32$. The precise value of Λ is not critical. Any neighboring value will produce similar results.

5. Main results

a. Pure-DI with $L_{\rm D}$ =1200 km, $q^*_{\rm max} = 16$, and varying bias

We focus on the pure-DI case with $L_{\rm D} = 1200\,$km, then comment briefly on similarities and differences for $L_{\rm D} = 1500\,$km and for midlatitude cases. Further details are given in Thomson (2015). It is for $L_{\rm D} = 1200\,$km, far below the A2 stability threshold, that we obtain the widest ranges of $q^*_{\rm max}$ and $b_{\rm max}$ over which model flows are realistic and statistically steady. Broadly speaking, the range of $q^*_{\rm max}$ values that produce such flows are found to be in or near the semi-strong regime.

Figures 3–7 show typical results for the pure-DI case with $L_{\rm D} = 1200\,$km and $q^*_{\rm max} = 16$.

In Fig. 3 the inner, dashed curve is the deep-jet velocity profile $\bar{u}_{\rm deep}(y) - U_0$. The solid curves are upper-jet profiles $\bar{u}(y)$ for different biases, after 120 yr (Earth years) of integration from the standard initialization. The model belt lies approximately within the y-interval between 2500 km and 7500 km, where the mean shears are cyclonic. Thus the central portion of Fig. 3 corresponds to the central portion of Fig. 1. The model zone is in the periphery and its periodic extension. The upper-jet profiles $\bar{u}(y)$ begin with the anticyclones-only run, $b = 1$ for all ζ. This is the first solid curve, heavier than the rest and only slightly different from the dashed curve. The lighter solid curves, peaking at successively higher values of $|\bar{u}|$, correspond to $b_{\rm max} =$ 1/4, 1/8, 1/16, 1/32, 1/64, and 0 respectively. We also ran $b_{\rm max} = 1/2$; the profile, not shown, hardly differs from the dashed curve and the heavy, $b = 1$ profile.

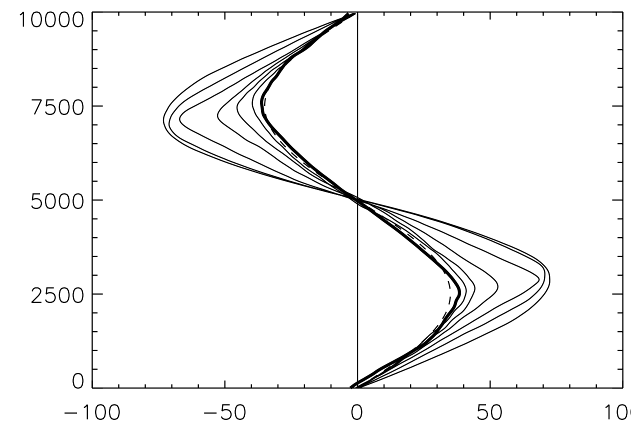

FIG. 3. Zonal-mean zonal velocity profiles for the pure-DI case with $L_{\rm D} = 1200\,$km and $q^*_{\rm max} = 16$, at time $t = 120$ Earth years. The inner, dashed curve is $\bar{u}_{\rm deep}(y) - U_0$. The heavy solid curve is the upper profile $\bar{u}(y)$ for the anticyclones-only run, $b = 1$ for all ζ. The lighter solid curves show $\bar{u}(y)$, in order of increasing peak $|\bar{u}|$, respectively for $b_{\rm max} =$ 1/4, 1/8, 1/16, 1/32, 1/64, and 0.

Evidently the actual mean shears in the model belt are either close to, or somewhat greater in magnitude than, the nominal value $U_{\rm max}/L$ in (4.2). So with $q^*_{\rm max} = 16$ only just greater than Kida's number 13.443, most injections are semi-strong. A small minority can be strong, depending on injection locations, as further discussed below in connection with an illustrative movie.

As anticipated, reducing the bias reduces the quasifrictional effect of $\bar{F}$, allowing stronger upper jets. In this pure-DI case there is no dynamical difference between prograde and retrograde jets, which on average are sharpened and strengthened by the same amounts.

The runs with $b_{\rm max}$ from 1/4 to 1/16, and the run with $b = 1$, are all close to statistical steadiness, consistent with the flattening-out of the corresponding curves in Fig. 4. These give domain-averaged total energy in ${\rm J kg^{-1}}$ against time t, with bias decreasing upward from curve to curve. Total energies are dominated by $\frac{1}{2}|\bar{u}|^2 + \frac{1}{2}k_{\rm D}^2|\bar{\psi}|^2$, the

[7] The number 13.443 is easily verified from the first line of Kida's Eq. (3.4), by setting $s = 1$ and plotting the right-hand side over an interval $r \in (0, 1)$. In Kida's notation $r = 1$ corresponds to a circular vortex and $r = 0$ to a vortex shredded by the shear into an infinitely thin filament. Taking $s = 1$ picks out the case of an initially circular vortex. The vortex is shredded if for all r the right-hand side of Kida's (3.4) stays between ± 1, while if it dips below -1 the vortex survives. For pure adverse shear such a dip occurs whenever, in Kida's notation, $\omega/e = -\omega/\gamma > 13.4430$, where $\omega = \frac{1}{2}|q_{\rm pk}|$ and $|\gamma|$ is half the shear. For pure favorable shear there is no sharp threshold, but for instance $0 < \omega/e = \omega/\gamma < 1$ makes an initially circular vortex shear out to aspect ratios beyond 25. Its destruction is then a practical certainty for finite $L_{\rm D}$, or for almost any background differing from Kida's strictly steady, strictly constant pure shear of infinite spatial extent.

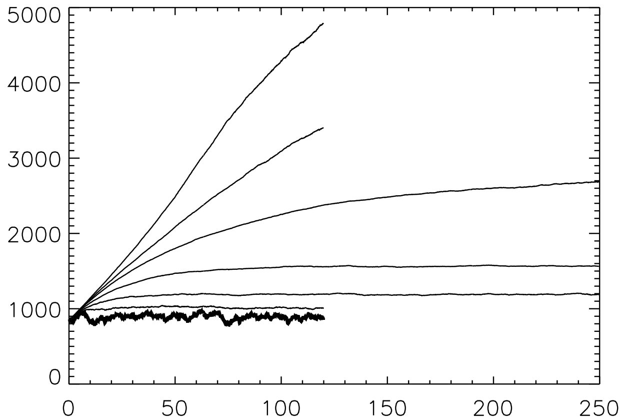

FIG. 4. Domain-averaged total energy per unit mass, in $\mathrm{J\,kg^{-1}}$ or $\mathrm{m^2 s^{-2}}$, against time in Earth years for the pure-DI case with $L_\mathrm{D} = 1200\,\mathrm{km}$ and $q^*_\mathrm{max} = 16$. The lowest, heavy solid curve is for the anticyclones-only run, $b = 1$ for all ζ. The lighter solid curves, reaching successively higher energies, correspond respectively to $b_\mathrm{max} =$ 1/4, 1/8, 1/16, 1/32, 1/64, and 0.

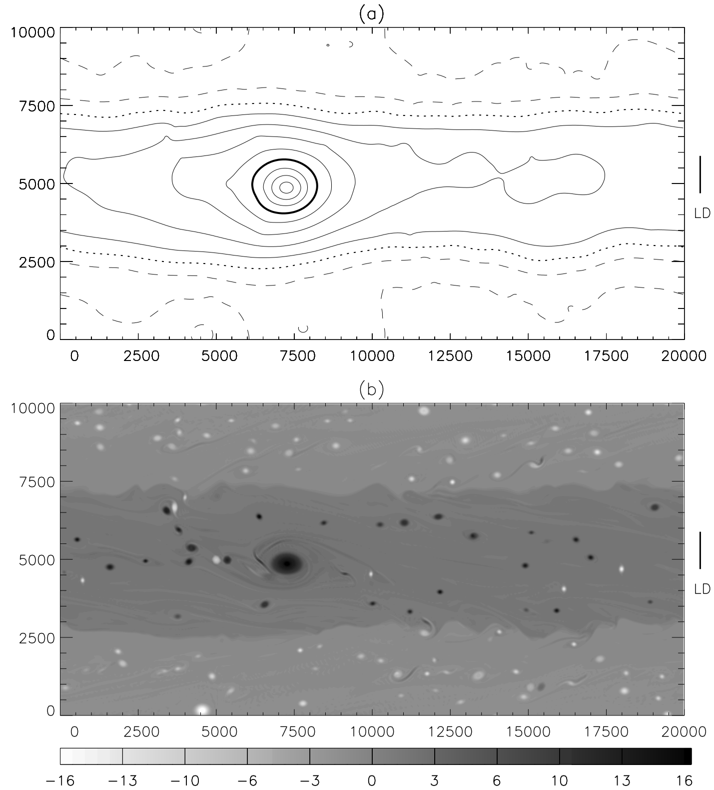

FIG. 5. Snapshots of the ζ and q fields at time $t = 120$ Earth years, in the pure-DI case with $L_\mathrm{D} = 1200\,\mathrm{km}$, $q^*_\mathrm{max} = 16$, and $b_\mathrm{max} = 1/16$. In the top panel (a), dashed contours show negative ζ and solid contours positive ζ, with contour interval 0.1 in the dimensionless units of Fig. 2. The heavy solid contour marks the value $\zeta = +0.5$ at which the ramp function $\rho(\zeta)$ saturates. In the bottom panel (b), which is the first frame of the supplemental movie, the grayscale is in units of $U_\mathrm{max}/L = 2.199 \times 10^{-5}\,\mathrm{s}^{-1}$, like q^*_max. The strongest vortices slightly exceed the grayscale range, with the large cyclone in mid-belt, $y \simeq 5000\,\mathrm{km}$, peaking at $q = 17.8 U_\mathrm{max}/L$ and the largest anticyclone peaking at $q = -18.4 U_\mathrm{max}/L$, to the far south-south-west near $x \simeq 4500\,\mathrm{km}$. There is one other out-of-range vortex, the small cyclone north-north-west of the large cyclone, near $x \simeq y \simeq 6400\,\mathrm{km}$, which peaks at $q = 17.7 U_\mathrm{max}/L$.

kinetic plus available potential energy of the zonal-mean flow, contributing in roughly equal proportions. Domain-averaged eddy energies, not shown, are relatively small but also flatten out, for the runs in question. The run with $b_\mathrm{max} = 1/32$ corresponds to the topmost of the three energy curves that reach 250yr. It is evolving toward statistical steadiness but does not come close to it until something like 500yr of integration. The run with $b = 1$, included for comparison and contrast with Li et al. (2006) and Showman (2007), is statistically steady apart from a decadal-timescale vacillation (heavy curve at bottom of Fig. 4). However, in that run the upper jets are hardly stronger than the deep jets, as seen in Fig. 3, and the ζ structure is correspondingly unrealistic.

b. A realistic example

We focus on the run for $b_\mathrm{max} = 1/16$. Fig. 5 shows snapshots of ζ in contours and q in grayscale for that run, at time $t = 120$yr. A corresponding q-field movie is provided in the online supplemental material, in grayscale and color versions. The bars on the right show L_D. Solid contours in Fig. 5a show positive ζ, a cold, elevated interface that increases moist-convective activity. The heavy solid contour marks the value $\zeta = +\frac{1}{2}$ at which the ramp function $\rho(\zeta)$ saturates. Dashed contours show negative ζ, a warm, depressed interface that reduces moist-convective activity. The structure of this ζ field is sufficiently zonal to count as realistic, by our criterion that the model should reflect the real planet's preference for stronger convection in belts than in zones.

The q snapshot in Fig. 5b is dominated by small vortices, produced by injections followed by migration — especially of small anticyclones from the belt into the zone — as well as by occasional vortex merging and other interactions. Cyclones are shown dark and anticyclones light. The small vortices move around chaotically, under their neighbors' influence and that of the background shear. Yet vortex merging and upscale energy cascading are inhibited to a surprising extent. This lack of upscale cascading will be discussed further in Section 6.

Conspicuous in Fig. 5b is a single, relatively large cyclone near $x \simeq 7500\,\mathrm{km}$ and $y \simeq 5000\,\mathrm{km}$. The strength of this cyclone fluctuates but is statistically steady. The snapshot shows it slightly larger and stronger than average. The strength is governed by a competition between vortex merging, cannibalism, and internal migration, on the one hand (Section 6 below), and attrition by local erosion and quasifrictional effects, on the other. The cyclone is strong enough to produce a conspicuous footprint in the ζ field, superposed on the quasi-zonal structure (Fig. 5a). The footprint takes the form of a cold patch or elevated area extending outward from the core of the cyclone on the lengthscale L_D.

The velocity field of the large cyclone modifies the background shear and strain quite substantially, such that some of the nearby injection events are strong rather than semi-strong. An example can be seen in the movie, starting west-south-west of the large cyclone at $t_{rel} = 0.408$, where time t_{rel} runs from 0 to 1 in units of movie duration, just under an Earth month. The injected anticyclone survives as it travels around the large cyclone, protected by the cyclone's *anticyclonic* angular shear, then slowly migrates into the model zone to the north, across the retrograde jet. The accompanying cyclone, caught in the same anticyclonic angular-shear environment, suffers partial erosion almost immediately after injection. It has a much shorter lifetime and ends up completely shredded, at $t_{rel} \simeq 0.58$, after one more partial erosion event.

Another clear example of migration from belt to zone, this time southward, occurs between $t_{rel} \simeq 0.65$ and $t_{rel} \simeq 0.9$. A recently-injected anticyclone partly merges with a pre-existing anticyclone, near $x \simeq 15000$ km and $y \simeq 3000$ km, and then migrates from belt to zone across the southern, prograde jet.

The snapshot in Fig. 5b is taken at the start of the movie, $t_{rel} = 0$. At that instant, there has just been an injection almost due west of the large cyclone, near $x \simeq 5000$ km. That injection proves to be semi-strong. Its anticyclone, seen on the left in Fig. 5b, is shredded immediately. However, its cyclone is also shredded shortly afterward, again by the anticyclonic angular-shear environment. During the cyclone's short lifetime ($t_{rel} \lesssim 0.13$), it migrates inward through a small radial distance, as can be checked by comparing its positions south and then north of the large cyclone, at $t_{rel} = 0.040$ and 0.098 respectively. Such events are frequent and are clearly part of what builds the large cyclone, whose typical q-structure is sombrero-like, a strong core surrounded by a weaker, fluctuating cyclonic PV anomaly, easier to see in the color movie than in the grayscale snapshot. That structure is alternately built up and eroded by a chaotic sequence of vortex interactions and injections.

Also notable in the movie is an injection making a rare direct hit on the inner core of the large cyclone, at $t_{rel} = 0.044$. Thanks to the condition (3.8) this injection behaves as a semi-strong injection. In this case the injected anticyclone is shredded into a tight spiral and acts quasifrictionally. By contrast, the injected cyclone stays almost completely intact, and migrates through a small radial distance to the center. The net effect is a slight reduction in the overall size and strength of the large cyclone, from above average to below average.

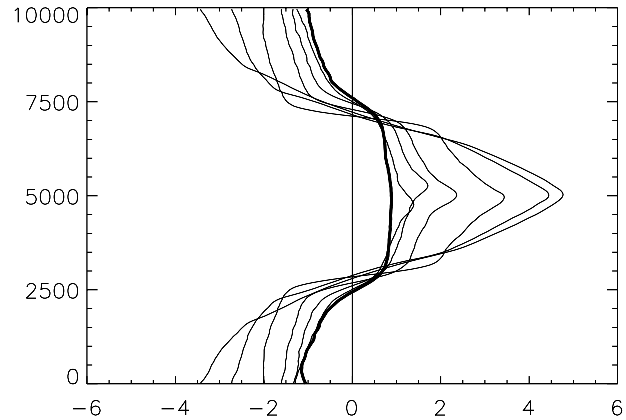

FIG. 6. Zonal-mean PV profiles $\bar{q}(y)$ for the pure-DI case with $L_D =$ 1200 km and $q^*_{max} = 16$, in units of $U_{max}/L = 2.199 \times 10^{-5}\,s^{-1}$, and time-averaged from $t = 115$yr to $t = 125$yr to reduce fluctuations. The heavy curve is the $\bar{q}(y)$ profile for the anticyclones-only run, $b = 1$ for all ζ, and the lighter curves with increasingly large peak $|\bar{q}|$ values correspond respectively to $b_{max} = 1/4$, 1/8, 1/16, 1/32, 1/64, and 0. The initial profile, not shown, is sinusoidal with amplitude 1 unit, its central peak only just beyond the flat part of the $b = 1$ heavy curve.

c. Varying bias again

Most of the statistically steady runs produce a single, relatively large cyclone in a similar way. Its average size increases as b_{max} and quasifriction are reduced. The runs with $b_{max} = 1/64$ and 0 were terminated at $t =$ 120yr because by then they had developed single cyclones large enough to produce an unrealistic, grossly nonzonal, footprint-dominated ζ structure.

The sharpened peaks of the jet profiles for $b_{max} =$ 1/16 in Fig. 3 correspond to sharp steps in the q field, as seen in Fig. 5b as sharp transitions between light gray and darker gray. These PV steps, embedded as they are in relatively uniform surroundings, resemble the cores of terrestrial strong jets apart from their relatively limited meandering, which is much more Jupiter-like. The formation of such steps from an initially smooth q field points to PV mixing across belts and zones as a contributing mechanism. A role for PV mixing is consistent with the chaotic appearance of the small-scale vortex interactions.

The PV steps persist into the two regimes with the smallest b_{max} values 1/64 and 0 and the largest cyclones. However, the PV steps are no longer reflected in the corresponding $\bar{u}(y)$ profiles in Fig 3, the outermost two profiles. Being Eulerian means, they are more rounded simply because the large cyclones make the jets meander more strongly. A Lagrangian mean, not shown, would follow the meandering and still reveal sharpened jet profiles — indeed even sharper than the sharpest in Fig. 3.

Figure 6 shows the Eulerian-mean $\bar{q}$ profiles for the

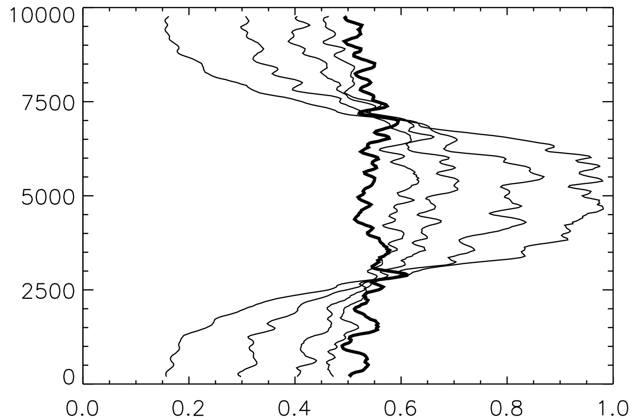

FIG. 7. Moist-convective activity in the model for the pure-DI case with $L_D = 1200\,\text{km}$, $q^*_{\max} = 16$, as measured by zonal mean strength-weighted injection frequencies $\bar{A}(y)$; see text. The heavy curve is for the anticyclones-only run $b = 1$. The lighter curves are for $b_{\max} = 1/4$, 1/8, 1/16, and 1/32, peaking successively further to the right. The small wiggles arise from the statistical fluctuations in the vortex-injection scheme, showing up despite time-averaging from 60 to 120 yr.

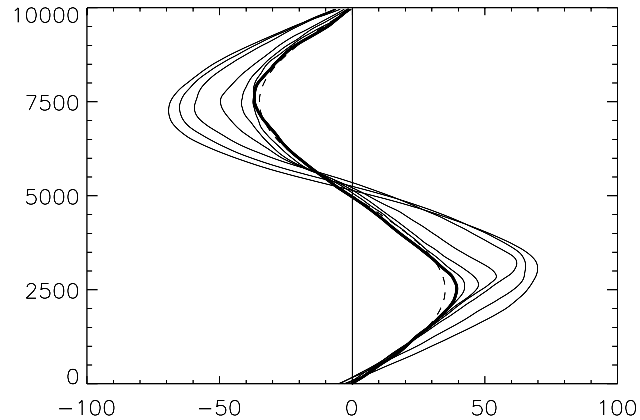

FIG. 8. Zonal-mean zonal velocity profiles for the midlatitude case with $L_D = 1200\,\text{km}$ and $q^*_{\max} = 16$, at time $t = 120$ Earth years, as in Fig. 3. Note that *all* the retrograde jet profiles are rounded.

same set of pure-DI runs, at time $t \simeq 120\text{yr}$ (see caption). For $b_{\max} \geqslant 1/16$, the profiles reflect the same inhomogeneous-PV-mixing structure, though the large cyclone in Fig. 5b creates a noticeable blip near $y \simeq 5000\,\text{km}$, in the $\bar{q}$ profile for $b_{\max} = 1/16$. Similar blips, corresponding to larger cyclones, become strong and then dominant as $b_{\max}$ is reduced to 1/32, 1/64, and 0; and the large cyclones are still growing in those runs. It is interesting to see what looks like a similar PV-mixing signature even for $b = 1$, the heavy curve, although the departure from the initial, sinusoidal $\bar{q}(y)$ profile is then very weak (see figure caption), and unable to produce a realistic ζ field.

Figure 7 gives an alternative view of the model's belt–zone structure for $b_{\max} \geqslant 1/32$. It shows a measure $\bar{A}$ of gross zonal-mean injection strength, time-averaged from 60yr to 120yr as well as zonally averaged, and computed as the mean $|\Delta q|$ of injected anticyclonic cores (3.1), ignoring their cyclonic companions and complementary forcings. Thus, $\bar{A} = 0$ would signal a complete absence of injections. Increasing values signal increasingly strong injections, on average, regardless of bias. The wiggles in the curves arise from the statistical fluctuations in the vortex-injection scheme. The belt-to-zone variation in injection strength seen in Fig. 7 is consistent with the realistic ζ structures found for moderately small values of $b_{\max}$, with the strongest injections concentrated in mid-belt. The unrealistic ζ structure for $b = 1$ produces, as expected, relatively little belt-to-zone variation in injection strength (heavy curve). The belt-to-zone variation increases as $b_{\max}$ decreases toward 1/32, but then decreases again (not shown) because of the dominance of the large cyclone, within which the condition (3.8) weakens the injections.

d. Other cases and parameter values

A corresponding set of results for $q^*_{\max} = 8$ (not shown; see Thomson 2015) shows similar behavior, though the tendency to form large cyclones is weaker, and there are cases in which the largest cyclones come in pairs. Most injections are then weak or semi-strong. For $q^*_{\max} = 32$, by contrast, many injections are strong, resulting in relatively violent vortex activity. A long run has been carried out for $q^*_{\max} = 32$ and $b_{\max} = 1/16$. It shows unrealistic, strongly nonzonal ζ structure, briefly described at the end of Section 6. For $q^*_{\max} = 1$ or less, practically all injections are weak. The response is then governed mainly by the Kelvin and $\bar{F}$ mechanisms. See Section 7.

For the "midlatitude" case, with $\beta - k_D^2 U_0 = 4.03 \times 10^{-12}\,\text{s}^{-1}\text{m}^{-1}$, the value of β itself at latitude 35°, the results (Thomson 2015) are broadly similar except that jet-sharpening is more effective for the prograde than for the retrograde jets. The $\bar{u}$ and $\bar{q}$ profiles for $L_D = 1200\,\text{km}$ and $q^*_{\max} = 16$ at time $t \simeq 120\text{yr}$ are shown in Figs. 8 and 9 (see captions). Again, only the runs with $b = 1$ or $b_{\max} \geqslant 1/16$ are close to statistical steadiness at $t \simeq 120\text{yr}$. Notice from Fig. 9 that the $\bar{q}$ profiles are still strongly nonmonotonic. The ζ and q fields for $b_{\max} = 1/16$ are similar to those in Fig. 5, except that the PV step near $y = 7500\,\text{km}$ is distinctly weaker, and the large cyclone distinctly stronger. Concomitantly, the ζ field is somewhat less zonal, with a stronger and larger cyclonic footprint.

The pattern of results for $L_D = 1500\,\text{km}$ is again broadly similar, except that realistic quasi-zonal structure is more easily disrupted. Vortex interactions reach across somewhat greater distances, and the whole system is somewhat closer to A2 marginality. This makes the jets somewhat

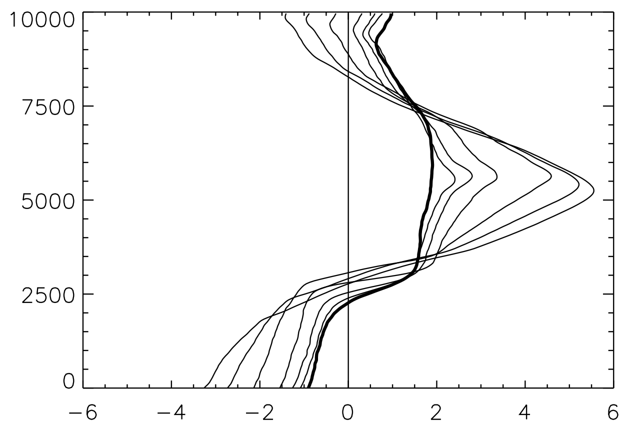

FIG. 9. Zonal-mean PV profiles $\bar{q}(y)$ for the midlatitude case with $L_{\rm D} = 1200\,\rm km$ and $q^*_{\rm max} = 16$, in units of $U_{\rm max}/L = 2.199\times10^{-5}\,\rm s^{-1}$, and time-averaged from $t = 115\rm yr$ to $t = 125\rm yr$ to reduce fluctuations. Biases vary as in Fig. 6. The background PV gradient 4.03×10^{-12} $\rm s^{-1}m^{-1}$ makes each profile shear over, with total displacement 1.83 units ($4.03 \times 10^{-12}\,\rm s^{-1}m^{-1} \times 10^7\,m \div 2.199 \times 10^{-5}\,s^{-1} = 1.83$).

more liable to large-scale meandering. The most realistic ζ fields are obtained for a narrower range of $q^*_{\rm max}$ values, closer to 8 than 16. For further detail see Thomson (2015).

e. Regarding statistical steadiness

As an extreme test of statistical steadiness, we ran our main case out to $t = 600\rm yr$ (pure DI, $q^*_{\rm max} = 16$, $L_{\rm D} = 1200\,\rm km$, $b_{\rm max} = 1/16$), and compared details with the 120-yr results shown above. All the mean profiles remain nearly indistinguishable from those in Figs. 3, 6, and 7, especially after a modest amount of time averaging. The PV snapshots are very similar to Fig. 5b, and in particular the largest cyclone and anticyclone both have similar sizes. As a further check, we produced a time series of domain-maximum cyclone strength over the whole time interval from $t = 0$ to $600\rm yr$. The time series showed fairly strong fluctuations, mostly in the range 15–20 in units of $U_{\rm max}/L$. Many of these fluctuations are fleeting and are, we think, due to transient Gibbs fringes produced by the high-wavenumber filter, during interactions involving the strongest small cyclones. The main point, however, is that the time series looks statistically steady from $t \simeq 100\rm yr$ onward, all the way out to 600yr.

6. Mechanisms in play

Vortex merging and upscale energy cascading are often taken for granted as central to all two-dimensionally turbulent flows. It therefore came as a surprise to us to discover the relative unimportance of those mechanisms in our most realistic cases, in which the stochastic forcing is nevertheless strong enough to produce chaotic vortex interactions. One reason is the sparseness of our vortex injection scheme, idealizing the intermittency of real Jovian moist convection as in Li et al. (2006). This contrasts with the extremely dense forcing — dense both spatially and temporally — used in beta-turbulence studies. They use a spatially dense forcing of a special kind, in order to achieve spectral narrowness (e.g., Srinivasan and Young 2014, Eq. (20) and Fig. 1f).

Sparse forcing need not, by itself, lead to sparse vortex fields, in a model with numerical dissipation small enough to allow long vortex lifetimes. For isolated strong vortices, injected with our standard size $r_0 = 4\Delta x$ into favorable shear, and with strength 16 times the shear, we find that lifetimes under numerical dissipation alone are typically of the order of years, albeit variable because they depend on the Robert filter and on bulk advection speeds across the grid. For comparison, average injection rates are of the order of 4 pairs per day in all the cases just described; and so the modest number of small vortices seen in snapshots like Fig. 5b can be explained only if vortex lifetimes are more like months than years. Vortex lifetimes are therefore limited not by numerical dissipation but by the chaotic vortex interactions themselves, as already illustrated by the erosion and shredding events seen in the q-field movie discussed in Section 5b.

The background shear and nonmonotonic PV gradients, imposed by the deep jets and the quasifrictional effect of $\bar{F}$ in our model, take us still further from a standard beta-turbulence scenario. Vortex-merging events do occur, as already noted, but require extremely close encounters and are much rarer than vortex erosion events.

The longest-lived small vortices are the anticyclones in the zone, shown white in Fig. 5b. Of these, the weakest come from local injections, corresponding to low values of the ramp function $\rho(\zeta)$, and the strongest from migration events like the two described in Section 5b. Such migration, of small but relatively strong anticyclones from belt to zone, can be attributed to a combination of chaotic, quasi-random walking away from strong-injection sites on the one hand, and the so-called "beta-gyre" mechanism on the other.

As is well known, and as we have verified by experimentation with our model, a single vortex injected into a background PV gradient will immediately advect the background gradient to produce a pair of opposite-signed PV anomalies on either side, traditionally called "beta-gyres", whose induced velocity field advects the original vortex toward background values closer to its own PV values. This migration mechanism weakens as the anomalies wrap up into a spiral pattern around the original vortex. Nevertheless, the mechanism appears to have a role in helping an anticyclone to cross a jet, from belt to zone either northward or southward. Such an anticyclone typically carries with it a wrapped-up cyclonic fringe, which is subsequently eroded away.

The range of anticyclone sizes and strengths illustrated in Fig. 5b, up to the largest anticyclone near the bottom of the figure near $x \simeq 4500\,\text{km}$, shows that there must have been occasional merging events during the preceding 120 yr. As already emphasized, however, most vortex encounters produce erosion rather than merging. The outcome is statistical steadiness with no further net growth of the largest anticyclone, even over 600yr, though it remains an open question whether further such growth occurs in realistic parameter ranges as yet unexplored, for instance with larger r_0 or injections less sparse.

The inward migration of injected cyclones within a larger cyclone plays a role in the buildup and persistence of the large cyclones we observe. For instance the example in the movie between $t_{\rm rel} \simeq 0.04$ and 0.10 (Section 5b) does, on close inspection, show a local beta-gyre mechanism in operation, the neighboring PV contours being weakly twisted in the sense required, as is especially clear around $t_{\rm rel} \simeq 0.10$. The corresponding mechanism for large anticyclones seems too weak to compete with erosion, in the regimes explored so far that have realistic ζ structure.

For brevity, no profiles of $\overline{v'q'}$ and $\partial(\overline{v'q'})/\partial y$ are shown here. Their qualitative characteristics are, however, simple, and easy to see for realistic, statistically steady states like that of Fig. 5. For then, broadly speaking, ζ and b are maximal in mid-belt and minimal in mid-zone, having regard to (3.5) and to quasi-zonal ζ fields like that in Fig. 5a. In a statistically steady state the right-hand side of (2.8) must vanish, after time-averaging over any vacillations. Thus averaged, $\partial(\overline{v'q'})/\partial y$ must therefore have the same y-profile as $\bar{F}$. Apart from a sign reversal and an additive constant, such $\bar{F}$ profiles are shaped like smoothed versions of the profiles of $\bar{A}$ in Fig. 7, in realistic cases, though $-\bar{F}$ tends to be more strongly peaked in mid-belt because of the dependence (3.5) of b upon ζ. The additive constant is required in order to make $\int_0^{2\pi L} \bar{F}\, dy = 0$, for consistency with (2.6b).

Periodicity and the Taylor identity (2.9) require, moreover, that $\int_0^{2\pi L} \overline{v'q'}\, dy = 0$. The $\overline{v'q'}$ profile therefore has to be qualitatively like an additive constant plus the periodic part of the indefinite integral of $-\bar{A}(y)$. Again after suitable time-averaging this is a smooth, quasi-sinusoidal curve going positive to the south and negative to the north of mid-belt, which is consistent with the migration of strong anticyclones from belt to zone already noted. Both $\overline{v'q'}$ and $\overline{u'v'}$ are upgradient at nearly all latitudes, in pure-DI cases. Explicit diagnostics of the model output confirm this qualitative picture (Thomson 2015). There is no PV-mixing signature in the statistically steady state if only because, as illustrated in Fig. 5b, the mixing has already taken place.

The pure-DI run with $q^*_{\max} = 32$ (for details again see Thomson 2015) develops not only a large cyclone but also a large anticyclone, perhaps reminiscent of the real planet's

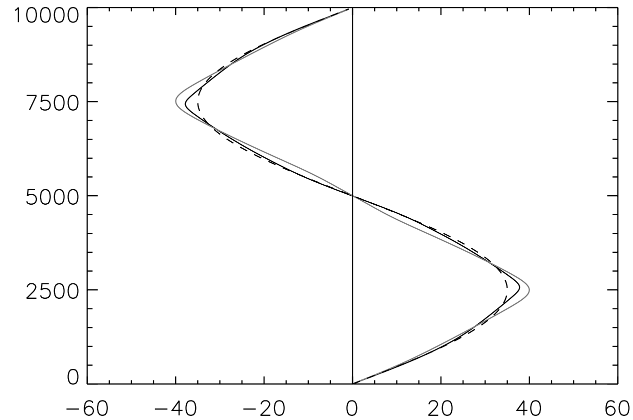

FIG. 10. Zonal-mean zonal velocity profiles $\bar{u}(y)$ for a pair of Kelvin-dominated, pure-DI runs with $L_{\rm D} = 1200\,\text{km}$ and $q^*_{\max} = 0.5$ (darker solid curve) and $q^*_{\max} = 1.0$ (lighter solid curve), with $b_{\max} = 1/64$ and with injection rates $t^{-1}_{\max}$ increased by a factor 100; see text. Although it makes little difference to these profiles, they have been time-averaged from $t = 108$ to 202 Earth years for consistency with the profiles of $\bar{\zeta}$, $\bar{q}$, and $\bar{A}$ shown below, some of which are more subject to fluctuations within a statistically steady state. The dashed curve is the deep-jet velocity profile $\bar{u}_{\rm deep}(y) - U_0$ as before.

Ovals, although more symmetrically located within the model zone. There are two more caveats. First and most important, the accompanying ζ structure is footprint-dominated, and not quasi-zonal as in Fig. 5a. So we count it as unrealistic. The model's large anticyclone depends less on belt-to-zone migration than on strong injections directly into the zone.

Second, the two large vortices and their periodic images form a vortex street, more precisely a vortex lattice, constrained by the 2:1 geometry of the model domain. Without extending our study to a much larger domain we cannot, therefore, claim to be capturing possible vortex-street properties in any natural way.

7. The Kelvin mechanism

The Kelvin/CE2/SSST passive-shearing mechanism has gained increased attention recently (e.g., Srinivasan and Young 2014, and references therein). It is one of three very different mechanisms for creating and sharpening jets, the other two being the Rhines and PV-mixing mechanisms already mentioned. The Kelvin mechanism is simple to understand, especially when the weak forcing is anisotropic in the same sense as that of our injected vortex pairs, with their east-west orientation. Such pairs are immediately sheared into phase-tilted structures producing upgradient Reynolds stresses $\overline{u'v'}$. The Taylor identity (2.9) determines the accompanying $\overline{v'q'}$ field. That field describes an eddy PV flux that is upgradient at some latitudes y and downgradient at others and, as indicated by the y derivative in (2.9), involves subtle phase relations sensitive to the

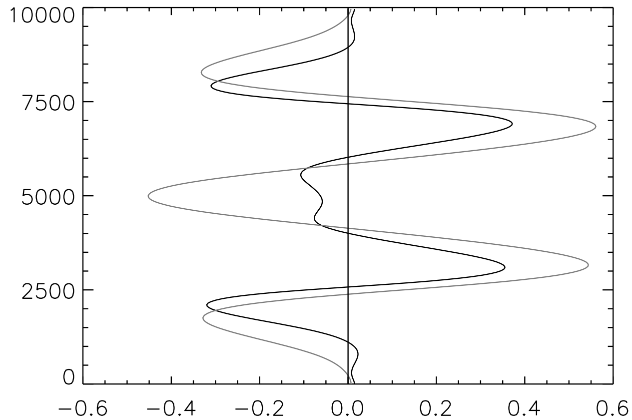

FIG. 11. Zonal-mean interface-elevation profiles $\bar{\zeta}(y)$ for the same pair of Kelvin-dominated runs, with $q^*_{\max} = 0.5$ (darker curve) and $q^*_{\max} = 1.0$ (lighter curve), both time-averaged from $t = 108$ to 202 Earth years as before. Without the time averaging, the $q^*_{\max} = 1.0$ curve would be less symmetric and would fluctate noticeably, because of vacillations mentioned in the text.

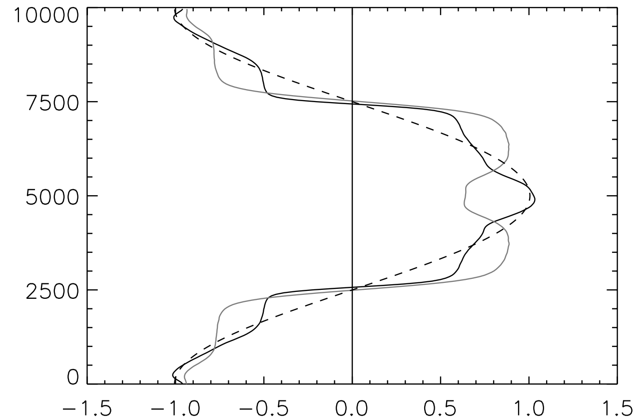

FIG. 12. Zonal-mean PV profiles $\bar{q}(y)$ for the same pair of Kelvin-dominated runs, with $q^*_{\max} = 0.5$ (darker solid curve) and $q^*_{\max} = 1.0$ (lighter solid curve), both time-averaged from $t = 108$ to 202 Earth years as before; see text. The dashed, sinusoidal curve is the initial PV profile.

y-gradients of disturbance amplitude and shearing rates.

To suppress small-scale vortex activity and to allow the Kelvin mechanism to dominate, we must take $q^*_{\max}$ small enough to ensure that injections are almost always weak. Figures 10–12 show statistically steady $\bar{u}$, $\bar{\zeta}$, and $\bar{q}$ profiles from a pair of pure-DI runs with $q^*_{\max} = 0.5$ and 1 (darker and lighter curves respectively). As before, we take $L_{\rm D} = 1200\,$km. The Kelvin mechanism is so weak that, in order to see it working and to reach statistical steadiness, we had to reduce $b_{\max}$ to 1/64 and to increase the average injection rate by two orders of magnitude, i.e., we had to reduce $t_{\max}$ by a factor 100.

The jets are indeed sharpened and the jet-core $\bar{q}$ profiles steepened, in both cases, creating in turn a $\bar{\zeta}$ structure that is interesting but unrealistic. As Fig. 11 shows, the central part of the belt is relatively warm, $\bar{\zeta}$ negative, with only the edges cold, $\bar{\zeta}$ positive. The corresponding $\bar{A}$ profiles are shown in Figure 13.

The unrealistic $\bar{\zeta}$ structure arises from the way the Kelvin mechanism works in a model with no artificial Rayleigh friction, corresponding to the low-friction limit found by Srinivasan and Young (2014), their $\mu \to 0$. Each sheared vortex-pair structure survives as long as it can, through nearly the whole range of phase-tilt angles. It is only when the orientation has become nearly zonal that the structure is destroyed by the model's high-wavenumber filter. Thus its lifetime is inversely proportional to the local background shear $\partial\bar{u}/\partial y$. The Reynolds stress $\overline{u'v'}$, time-averaged over many injections, is also, therefore, inversely proportional to $\partial\bar{u}/\partial y$, as in Eq. (44) of Srinivasan and Young (2014). So as long as the $\bar{u}$ profile remains close to its initially sinusoidal shape while the ζ field remains flat, keeping injection strengths uniform everywhere, the profile of $-\overline{u'v'}$ has a smooth, positive-valued U shape within the belt, with a broad minimum in mid-belt and a steep increase toward each jet extremum. In the zone, with the sign of $\partial\bar{u}/\partial y$ reversed, it is $+\overline{u'v'}$ rather than $-\overline{u'v'}$ that is positive and U-shaped; and there is a very steep transition at each jet extremum producing a sharp, narrow peak in the zonal force $-\partial(\overline{u'v'})/\partial y$, positive at the prograde jet and negative at the retrograde.

The jet-sharpening is therefore strongly localized, with a small y-scale $\ll L_{\rm D}$. It begins with narrow peaks growing at the extrema of the otherwise-sinusoidal $\bar{u}$ profile, with $|\partial\bar{u}/\partial y|$ reduced everywhere else. The PV profile develops correspondingly sharp steps, cut into the sides of its initially sinusoidal shape. That is, there is localized jet-sharpening but — in striking contrast with Fig. 3 — weakening rather than strengthening of $\bar{u}$ at most other latitudes y. The thermal-wind tilt of the interface is therefore, at most other latitudes, opposite to what it was in the cases discussed in Section 5, except within narrow regions near the jet peaks. That is the essential reason why the belt develops a warm, negative-$\bar{\zeta}$ central region with cold, positive-$\bar{\zeta}$ regions only in the outer parts of the belt.

The change in the y-profile of $\bar{\zeta}$ and hence of injection strengths then reacts back on the $\overline{u'v'}$ profiles, but in a rather smooth way that leaves the qualitative pattern unchanged. Indeed, the back-reaction acts as a positive feedback that *reinforces* the pattern, because the warm belt center weakens the injections there and thus deepens the central minimum in the U-shaped profile of $-\overline{u'v'}$. That is why the lighter curve in Fig. 10, corresponding to the less weakly forced run, $q^*_{\max} = 1$, shows a $\bar{u}$ profile more conspicuously weakened across most of the belt. The resulting thermal-wind tilt further reinforces the central warmth of the belt.

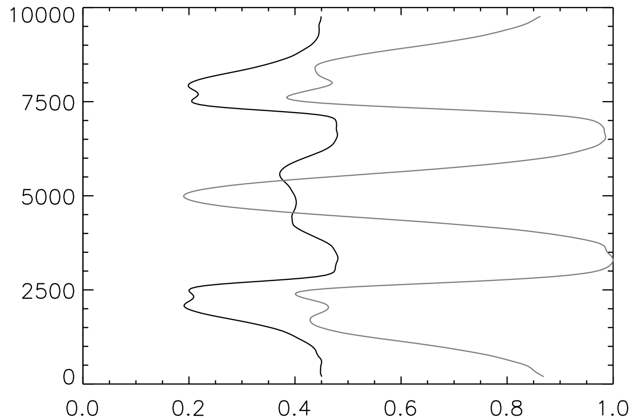

FIG. 13. Moist-convective activity profiles $\bar{A}(y)$ for the same pair of Kelvin-dominated runs, with $q^*_{\rm max} = 0.5$ (darker curve) and $q^*_{\rm max} = 1.0$ (lighter curve), both time-averaged from $t = 108$ to 202 Earth years as before. In the central part of the belt convective activity is inhibited, in both runs, for the reasons explained in the text.

The stronger feedback for $q^*_{\rm max} = 1$ appears to be responsible for the central dip in the $\bar{q}$ profile seen in the lighter curve in Figure 12. The central dip gives rise to a weak long-wave shear instability (though stronger when $L_{\rm D} = 1500\,{\rm km}$), because we then have nonmonotonic $\partial\bar{q}/\partial y$ on a smaller y-scale, putting pairs of counterpropagating Rossby waves within reach of each other. This long-wave instability produces vacillations in the form of weak traveling undulations with zonal wavenumber 1. The vacillations hardly affect the $\bar{u}$ and $\bar{q}$ profiles, but show up more clearly in a time sequence of $\bar{\zeta}$ profiles. The corresponding $\bar{\zeta}$ profile in Fig 11 (lighter curve) has been time-averaged to reduce the effects of these vacillations.

For $q^*_{\rm max} = 0.5$ we see a weak and entirely different, zonally symmetric, mode of instability that causes spontaneous y-symmetry breaking in the central region of the belt, $4000\,{\rm km} \lesssim y \lesssim 6000\,{\rm km}$. For instance the $\bar{u}$ profile given by the darker solid curve in Fig. 10 shows a tiny departure from antisymmetry about mid-belt. The darker curves in Figs. 11 and 13 are more conspicuously asymmetric in the central region. Considering a $\bar{u}$ profile consisting of a constant cyclonic shear plus a small wavy perturbation, we see that such a perturbation is zonostrophically stable — because the abovementioned inverse proportionality reduces $|\overline{u'v'}|$ wherever $|\partial\bar{u}/\partial y|$ increases — but "thermostrophically unstable" via the feedback from $\bar{\zeta}$, which evidently has the opposite effect on $|\overline{u'v'}|$ and predominates in this case.

8. Concluding remarks

In view of the Kelvin regimes' lack of realism we return to the model's realistic, statistically steady, pure-DI regimes that have been our main focus (Sections 5–6). In those regimes, not only is $\overline{u'v'}$ persistently upgradient, but also $\overline{v'q'}$, at nearly all latitudes y, after sufficient time averaging. The small-scale vortex activity produces a persistent migration of small anticyclones from belts to zones. The importance of such migration on the real planet was suggested by Ingersoll et al. (2000). In the model it is mediated by quasi-random walking away from strong-injection sites, via chaotic vortex interactions, in combination with the so-called beta-gyre mechanism (Section 6 above).

Both mechanisms are entirely different from the Kelvin mechanism because the latter involves no vortex interactions, as already emphasized, but only passive shearing of injected vortex pairs by the background zonal flow $\bar{u}(y)$. Passive shearing of small-scale anomalies is also what seems to produce the upgradient $\overline{u'v'}$ in the real planet's cloud-top winds (e.g., Salyk et al. 2006). Yet, in our model at least, as shown in Section 7, the Kelvin mechanism cannot produce a realistic ζ structure. It therefore cannot, in this model, produce a realistic belt-to-zone contrast in moist-convective activity.

We suggest therefore that the cloud-top $\overline{u'v'}$ on the real planet must be a relatively shallow phenomenon, whose vertical scale is much smaller than the depth of the weather layer. It is most likely, we suggest, to result not from the shearing of tall, columnar vortices resembling the injected vortices in our model but, rather, from the shearing of the real weather-layer's small scale, baroclinic, fully three-dimensional fluid motions. Such motions, including shallow vortices and the real filamentary moist convection are, of course, outside the scope of any $1\frac{1}{2}$-layer model and not simply related to PV fields like that of Fig. 5b above.

As is well known, the same conclusions are suggested by the absurdly large kinetic-energy conversion rates obtained when the cloud-top $\overline{u'v'}$ field is assumed to extend downward, along with $\partial\bar{u}/\partial y$, throughout the entire weather layer. When one vertically integrates cloud-top conversion rates $\overline{u'v'}\,\partial\bar{u}/\partial y$, whose global average $\sim 10^{-4}\,{\rm W kg^{-1}}$, then global integration gives numbers "in the range 4–8% of the total thermal energy emitted by Jupiter" (Salyk et al. 2006). Such large conversion rates are overwhelmingly improbable, in a low-Mach-number fluid system such as Jupiter's weather layer.

Consistent with these considerations, the model's flow regimes with realistic ζ structures have conversion rates $\overline{u'v'}\,\partial\bar{u}/\partial y$ that are still positive, but about two orders of magnitude smaller. For instance, in the case examined in Section 5b we find $\overline{u'v'}\,\partial\bar{u}/\partial y$ values that fluctuate around a time-mean close to $1 \times 10^{-6}\,{\rm W kg^{-1}}$ (Thomson 2015). Such values are much more plausible, for the whole weather layer, than the observed cloud-top values $\sim 10^{-4}\,{\rm W kg^{-1}}$.

Perhaps the weakest aspect of the current model is the artificial condition (3.8) that we adopted in order to avoid strong-cyclone runaway. As is well known, the real planet's large cyclones can be intensely convective, presumably because they have cold, high-ζ footprints. No $1\frac{1}{2}$-layer vortex-injection scheme can come close to representing the three-dimensional reality. An attractive compromise, and a possible way of dispensing with (3.8), might be to introduce an eddy viscosity whose value intensifies whenever and wherever the model's convective activity intensifies. This might capture some of the dissipative effects of the real, three-dimensionally turbulent moist convection, while still avoiding the use of Rayleigh friction or other such artifice.

A localized, convection-dependent eddy viscosity would have the advantage of, probably, allowing realistic statistically steady states with a simpler vortex-injection scheme, such as that described by Eqs. (3.2)–(3.7) alone. It could automatically expand the core sizes, and dilute the peak strengths, of the strongest injected vortices and thus prevent strong-cyclone runaway. As an added bonus it might even produce realistic cases in which large anticyclones form (cf. end of Section 6). Because the real planet's large anticyclones are not ubiquitous, there may be a certain delicacy about the conditions that allow them to form. Questions like these must await future studies.

Acknowledgements: Emma Boland and Andy Thompson kindly helped us with the model code. We also thank them for useful comments and and/or encouragement along with James Cho, David Dritschel, Tim Dowling, Leigh Fletcher, Boris Galperin, Thomas Gastine, Gary Glatzmaier, Peter Haynes, Xianglei Huang, Andy Ingersoll, Chris Jones, Kirill Kuzanyan, Junjun Liu, Inna Polichtchouk, Peter Read, Tapio Schneider, Richard Scott, Sushil Shetty, Adam Showman, Steve Tobias, Richard Wood, Bill Young, and Roland Young. We also thank the UK Science and Technology Facilities Council for financial support in the form of a research studentship.

REFERENCES

Asay-Davis, X. S., P. S. Marcus, M. H. Wong, and I. de Pater, 2009: Jupiter's shrinking Great Red Spot and steady Oval BA: velocity measurements with the 'Advection Corrected Correlation Image Velocimetry' automated cloud-tracking method. *Icarus*, **203**, 164–188, doi:10.1016/j.icarus.2009.05.001.

Bühler, O., 2014: *Waves and Mean Flows, 2nd edn.* University Press, Cambridge, 360 pp., doi:10.1017/CBO9781107478701.

Dowling, T. E., 1993: A relationship between potential vorticity and zonal wind on Jupiter. *J. Atmos. Sci.*, **50**, 14–22, doi:10.1175/1520-0469(1993)050⟨0014:ARBPVA⟩2.0.CO;2.

Dowling, T. E. and A. P. Ingersoll, 1989: Jupiter's Great Red Spot as a shallow water system. *J. Atmos. Sci.*, **46**, 3256–3278, doi:10.1175/1520-0469(1989)046⟨3256:JGRSAA⟩2.0.CO;2.

Gastine, T., M. Heimpel, and J. Wicht, 2014: Zonal flow scaling in rapidly-rotating compressible convection. *Phys. Earth Planet. Inter.*, **232**, 36–50, doi:10.1016/j.pepi.2014.03.011.

Guillot, T., 2005: The interiors of giant planets: models and outstanding questions. *Ann. Rev. Earth Planet. Sci.*, **33**, 493–530, doi:10.1146/annurev.earth.32.101802.120325.

Haynes, P. H. and M. E. McIntyre, 1990: On the conservation and impermeability theorems for potential vorticity. *J. Atmos. Sci.*, **47**, 2021–2031, doi:10.1175/1520-0469(1990)047⟨2021:OTCAIT⟩2.0.CO;2.

Hoskins, B., M. McIntyre, and A. Robertson, 1985: On the use and significance of isentropic potential-vorticity maps. *Quart. J. Roy. Meteorol. Soc.*, **111**, 877–946, doi:10.1002/qj.49711147002, see also *Corrigendum*, vol. **113**, 402–404 (1987), doi:10.1002/qj.49711347522.

Humphreys, T. and P. S. Marcus, 2007: Vortex street dynamics: the selection mechanism for the areas and locations of Jupiter's vortices. *J. Atmos. Sci.*, **64**, 1318–1333, doi:10.1175/JAS3882.1.

Ingersoll, A. and P. Cuong, 1981: Numerical model of long-lived Jovian vortices. *J. Atmos. Sci.*, **38**, 2067–2076, doi:10.1175/1520-0469(1981)038⟨2067:NMOLLJ⟩2.0.CO;2.

Ingersoll, A. P., P. J. Gierasch, D. Banfield, A. R. Vasavada, and the Galileo Imaging Team, 2000: Moist convection as an energy source for the large-scale motions in Jupiter's atmosphere. *Nature*, **403**, 630–632, doi:10.1038/35001021.

Ingersoll, A. P. and C. C. Porco, 1978: Solar heating and internal heat flow on Jupiter. *Icarus*, **35**, 27–43, doi:10.1016/0019-1035(78)90058-1.

Jones, C. A. and K. M. Kuzanyan, 2009: Compressible convection in the deep atmospheres of giant planets. *Icarus*, **204**, 227–238, doi:10.1016/j.icarus.2009.05.022.

Kida, S., 1981: Motion of an elliptic vortex in a uniform shear flow. *J. Phys. Soc. Japan*, **50**, 3517–3520, doi:10.1143/JPSJ.50.3517.

Li, L., A. P. Ingersoll, and X. Huang, 2006: Interaction of moist convection with zonal jets on Jupiter and Saturn. *Icarus*, **180**, 113–123, doi:10.1016/j.icarus.2005.08.016.

Limaye, S. S., 1986: Jupiter: New estimates of the mean zonal flow at the cloud level. *Icarus*, **65**, 335–352, doi:10.1016/0019-1035(86)90142-9.

Liu, J., T. Schneider, and Y. Kaspi, 2013: Predictions of thermal and gravitational signals of Jupiter's deep zonal winds. *Icarus*, **224**, 114–125, doi:10.1016/j.icarus.2013.01.025.

Marcus, P. S. and S. Shetty, 2011: Jupiter's zonal winds: are they bands of homogenized potential vorticity organized as a monotonic staircase? *Phil. Trans. Roy. Soc. Lond.*, **A 369**, 771–795, doi:10.1098/rsta.2010.0299.

Maximenko, N. A., B. Bang, and H. Sasaki, 2005: Observational evidence of alternating zonal jets in the world ocean. *Geophys. Res. Lett.*, **32**, L12 607, doi:10.1029/2005GL022728.

McIntyre, M. E. and T. G. Shepherd, 1987: An exact local conservation theorem for finite-amplitude disturbances to non-parallel shear flows, with remarks on Hamiltonian structure and on Arnol'd's stability theorems. *J. Fluid Mech.*, **181**, 527–565, doi:10.1017/S0022112087002209.

Porco, C. C., et al., 2003: Cassini imaging of Jupiter's atmosphere, satellites, and rings. *Science*, **299**, 1541–1547, doi:10.1126/science.1079462.

Read, P. L., P. J. Gierasch, B. J. Conrath, A. Simon-Miller, T. Fouchet, and Y. H. Yamazaki, 2006: Mapping potential-vorticity dynamics on Jupiter. I: Zonal-mean circulation from Cassini and Voyager 1 data. *Quart. J. Roy. Meteorol. Soc.*, **132**, 1577–1603, doi:10.1256/qj.05.34.

Salyk, C., A. P. Ingersoll, J. Lorre, A. Vasavada, and A. D. Del Genio, 2006: Interaction between eddies and mean flow in Jupiter's atmosphere: Analysis of Cassini imaging data. *Icarus*, **185**, 430–442, doi:10.1016/j.icarus.2006.08.007.

Scott, R. K. and D. G. Dritschel, 2012: The structure of zonal jets in geostrophic turbulence. *J. Fluid Mech.*, **711**, 576–598, doi:10.1017/jfm.2012.410.

Scott, R. K. and L. M. Polvani, 2007: Forced-dissipative shallow-water turbulence on the sphere and the atmospheric circulation of the giant planets. *J. Atmos. Sci.*, **64**, 3158–3176, doi:10.1175/JAS4003.1.

Shepherd, T. G., 1985: Time development of small disturbances to plane Couette flow. *J. Atmos. Sci.*, **42**, 1868–1871, doi:10.1175/1520-0469(1985)042⟨1868:TDOSDT⟩2.0.CO;2.

Shetty, S. and P. S. Marcus, 2010: Changes in Jupiter's Great Red Spot (1979–2006) and Oval BA (2000–2006). *Icarus*, **210**, 182–201, doi:10.1016/j.icarus.2010.06.026.

Showman, A. P., 2007: Numerical simulations of forced shallow-water turbulence: effects of moist convection on the large-scale circulation of Jupiter and Saturn. *J. Atmos. Sci.*, **64**, 3132–3157, doi:10.1175/JAS4007.1.

Showman, A. P. and I. de Pater, 2005: Dynamical implications of Jupiter's tropospheric ammonia abundance. *Icarus*, **174**, 192–204, doi:10.1016/j.icarus.2004.10.004.

Smith, K. S., G. Boccaletti, C. C. Henning, I. Marinov, C. Y. Tam, I. M. Held, and G. K. Vallis, 2002: Turbulent diffusion in the geostrophic inverse cascade. *J. Fluid Mech.*, **469**, 13–48, doi:10.1017/S0022112002001763.

Srinivasan, K. and W. R. Young, 2012: Zonostrophic instability. *J. Atmos. Sci.*, **69**, 1633–1656, doi:10.1175/JAS-D-11-0200.1.

Srinivasan, K. and W. R. Young, 2014: Reynolds stress and eddy diffusivity of β-plane shear flows. *J. Atmos. Sci.*, **71**, 2169–2185, doi:10.1175/JAS-D-13-0246.1.

Stamp, A. and T. E. Dowling, 1993: Jupiter's winds and Arnol'd's second stability theorem: slowly moving waves and neutral stability. *J. Geophys. Res.*, **98**, 18 847–18 855, doi:10.1029/93JE01520.

Sugiyama, K., K. Nakajima, M. Odaka, K. Kuramoto, and Y.-Y. Hayashi, 2014: Numerical simulations of Jupiter's moist convection layer: Structure and dynamics in statistically steady states. *Icarus*, **229**, 71–91, doi:10.1016/j.icarus.2013.10.016.

Sugiyama, K., M. Odaka, K. Kuramoto, and Y.-Y. Hayashi, 2006: Static stability of the Jovian atmospheres estimated from moist adiabatic profiles. *Geophys. Res. Lett.*, **33**, L03 201, doi:10.1029/2005GL024554.

Thomson, S. I., 2015: *A New Model of Jupiter's Jet Streams and the Effects of Moist Convection*. PhD Thesis, University of Cambridge, to be made available from the University Library, Superintendent of Manuscripts.

Thomson, W., 1887: (Lord Kelvin): Stability of fluid motion – rectilineal motion of viscous fluid between two parallel planes. *Phil. Mag.*, **24**, 188–196, doi:10.1080/14786448708628078.

Walterscheid, R., 2000: Wave disturbances from the Comet SL-9 impacts into Jupiter's atmosphere. *Icarus*, **145**, 140–146, doi:10.1006/icar.1999.6334.